Supplementary information

Identifying carbon as the source of visible single-photon emission from hexagonal boron nitride

Supplementary Information: Identifying Carbon as the Source of Visible Single Photon Emission from Hexagonal Boron Nitride

Noah Mendelson,[1] Dipankar Chugh,[2] Jeffrey R. Reimers,[1,3] Tin S. Cheng,[4] Andreas Gottscholl,[5] Hu Long,[6,7,8] Christopher J. Mellor,[4] Alex Zettl,[6,7,8] Vladimir Dyakonov,[5] Peter H. Beton,[4] Sergei V. Novikov,[4] Chennupati Jagadish,[2,9] Hark Hoe Tan,[2,9] Michael J. Ford,[1] Milos Toth,[1,10] Carlo Bradac,[1,11] Igor Aharonovich[1,10]*

[1]School of Mathematical and Physical Sciences, University of Technology Sydney, Ultimo, New South Wales 2007, Australia.
[2]Department of Electronic Materials Engineering, Research School of Physics and Engineering, The Australian National University, Canberra, Australian Capital Territory, Australia
[3]International Centre for Quantum and Molecular Structures and Department of Physics, Shanghai University, Shanghai 200444, China.
[4]School of Physics and Astronomy, University of Nottingham, Nottingham NG7 2RD, UK
[5]Experimental Physics 6 and Würzburg-Dresden Cluster of Excellence, Julius Maximilian University of Würzburg, Würzburg, Germany.
[6]Department of Physics, University of California, Berkeley, CA, USA.
[7]Materials Sciences Division, Lawrence Berkeley National Laboratory, Berkeley, CA, USA.
[8]Kavli Energy NanoSciences Institute at the University of California and the Lawrence Berkeley National Laboratory, Berkeley, CA, USA.
[9]ARC Centre of Excellence for Transformative Meta-Optical Systems, Research School of Physics and Engineering, The Australian National University, Australian Capital Territory, Australia
[10]ARC Centre of Excellence for Transformative Meta-Optical Systems, University of Technology Sydney, Ultimo, New South Wales, Australia.
[11] Department of Physics & Astronomy, Trent University, 1600 West Bank Dr., Peterborough ON, K9J 0G2, Canada

*Igor.Aharonovich@uts.edu.au

Supplementary Sections:

I. Additional characterization of epitaxial hBN samples
   a. Quantification to MOVPE carbon ensemble peak shapes
   b. Confocal mapping of epitaxially grown hBN samples
   c. Quantifying carbon incorporation during MOVPE growth *via* XPS
   d. Room Temperature ODMR from SPE ensembles in MOVPE (TEB 60)
   e. Emission energies of incorporated SPE zero-phonon lines in MOVPE and MBE samples

II. Additional characterization of implanted hBN samples
   a. Sample thickness of implanted hBN samples
   b. Additional data from carbon implanted hBN samples
   c. Analysis of SPEs created by carbon implantation

Supplementary Information I: Additional Characterization of Epitaxial hBN Samples

a. Quantification to MOVPE carbon ensemble peak shapes

***Figure S1—MOVPE hBN ensemble ZPL/PSB detuning. a.** An ensemble spectrum taken from MOVPE hBN (TEB 30) showing the energy separation between the ensemble of ZPLs to the resolved phonon sidebands. The detuning from the ZPL centroid at 2.122 eV to the LO_1 phonon mode at 1.961 eV is 161 meV. While the detuning from the ZPL to the LO_2 mode at 1.927 eV is 195 meV. **b.** An ensemble spectrum taken from a different confocal spot of the MOVPE hBN (TEB 30) sample where both the first and second order PSBs can be observed. The ZPL ensemble centroid is positioned at 2.116 eV, and the first PSB (which appears as a single peak due to the convolution of the LO_1 and LO_2 modes) is centered at 1.937 eV, a detuning of 179 meV. Additionally, a dimmer broad peak can be observed at lower energy spanning from roughly 1.789*

eV to 1.725 eV, corresponding to the second order phonon modes which are comprised of three independent emissions, $2LO_1$, LO_1+LO_2, and $2LO_2$.

Given the broad nature of the emission observed from MOVPE samples with triethyl boron (TEB) flow rates above 10 µmol/min, it is important to confirm the behavior of the photoluminescence is consistent with that of an ensemble of single photon emitters. We find a number of characteristics confirming this hypothesis. For example, the position of the ZPL lines changes slightly for different confocal spots, there are minor variations in the intensity of the ZPL and PSB on the scale of seconds in a single spot, consistent with certain emitters blinking on and off. Critically, the linewidth of the ensemble emission is consistent with the observed distribution of ZPL lines found from single emitters in the MOVPE hBN (TEB 10) sample, shown in Figure S5. Furthermore, the separation between the ZPL and $LO_{1\&2}$ modes, which comprise the typical first order phonon sideband in hBN, show the expected energetic separation known in the literature.[1, 2] Figure S1a, demonstrates that in particular confocal spots we can resolve the individual LO phonon modes, with energetic separations of ~161 meV and ~195 meV from the ZPL to the LO_1 and LO_2 phonon respectively. As seen in Figure S1b, other confocal spots clearly display the 2nd order phonon modes as well. The 2nd order PSB is comprised of the three individual peaks, the $2LO_1$, LO_1+LO_2, and $2LO_2$ modes, found at ZPL energy detuning values of ~330 meV, ~360 meV, and ~390 meV respectively.[1, 2] Consistent with this distribution we find the resolvable 2nd order PSB to span ~64 meV, and first appearing at ~327 meV downfield from the ZPL.
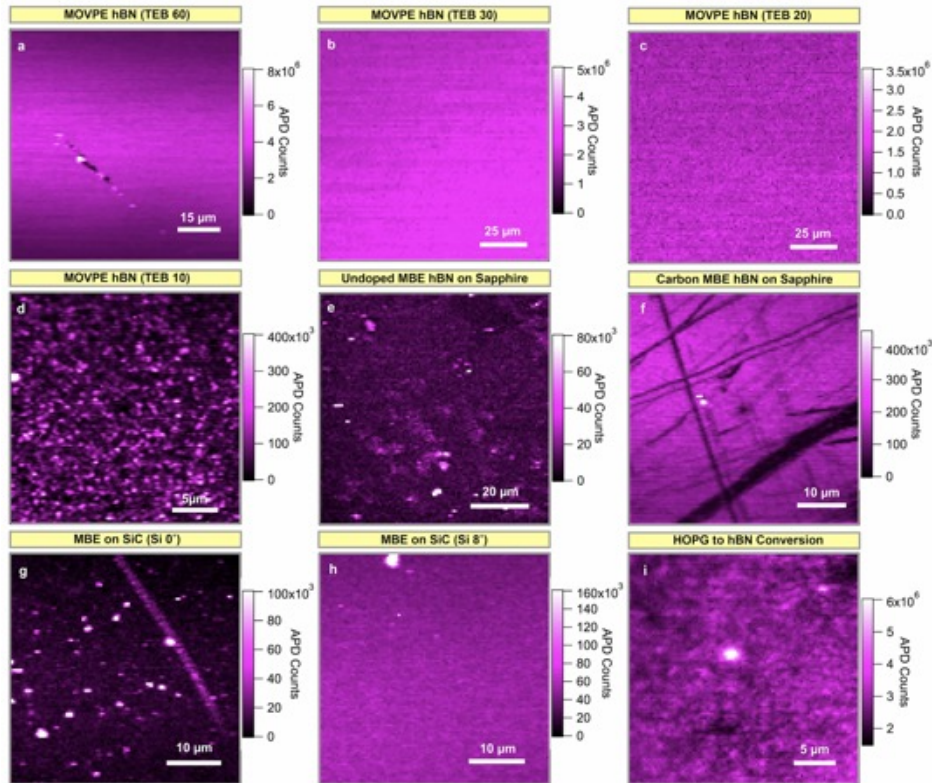
b. Confocal mapping of epitaxially grown hBN samples

Figure S2—Confocal scans of epitaxial hBN sources investigated. All confocal scans were taken with a 532 nm excitation source at a power of 100µW. **a.** MOVPE hBN (TEB 60). **b.** MOVPE hBN (TEB 30). **c.**

MOVPE hBN (TEB 20). **d.** MOVPE hBN (TEB 10). **e.** Undoped MBE hBN on sapphire. **f.** Carbon doped MBE hBN on sapphire. **g.** Undoped MBE hBN on silicon carbide with the silicon face at ~ 0˚. **h.** Undoped MBE hBN on silicon carbide with the silicon face at ~ 8˚. **i.** HOPG to hBN conversion.

Figure S2 displays the confocal scans of the 9 epitaxially grown samples types investigated. Each was recorded with a 532 nm excitation source at a power of 100µW. Figure S2a-c display the scans of the MOVPE samples with TEB flows of 60/30/20 µmol/min. Each demonstrates a consistent fluorescence intensity across the sample surface, decreasing according to the associated TEB flow. This finding is consistent with a homogeneous incorporation of SPE ensembles in these samples. Figure S2d demonstrates isolated bright spots within the film, corresponding to single photon emitters. Figure S2e&f display the confocal scans of MBE grown hBN on sapphire with and without a carbon source respectively. In the absence of a carbon source, a very low level of emission is observed, while the presence of a carbon source increases the fluorescence intensity by approximately 4-fold. In figure S2g&h, a similar trend is observed for the MBE growths on SiC, where a low emission intensity is observed for the SiC growth with the Si face oriented at 0˚, while a noticeable increase in observed for growth on SiC with the Si face oriented at 8˚. In the MBE samples showing SPE incorporation (Figure Sf&h) we see a relatively homogeneous fluorescence from the samples, consistent with the high density of incorporated emitters. Figure S2i shows a confocal scan of the HOPG to hBN conversion sample, which demonstrates a high emission intensity across the sample surface. The variation in intensity is primarily due to porous nature of the sample.

c. Quantifying carbon incorporation during MOVPE growth *via* XPS
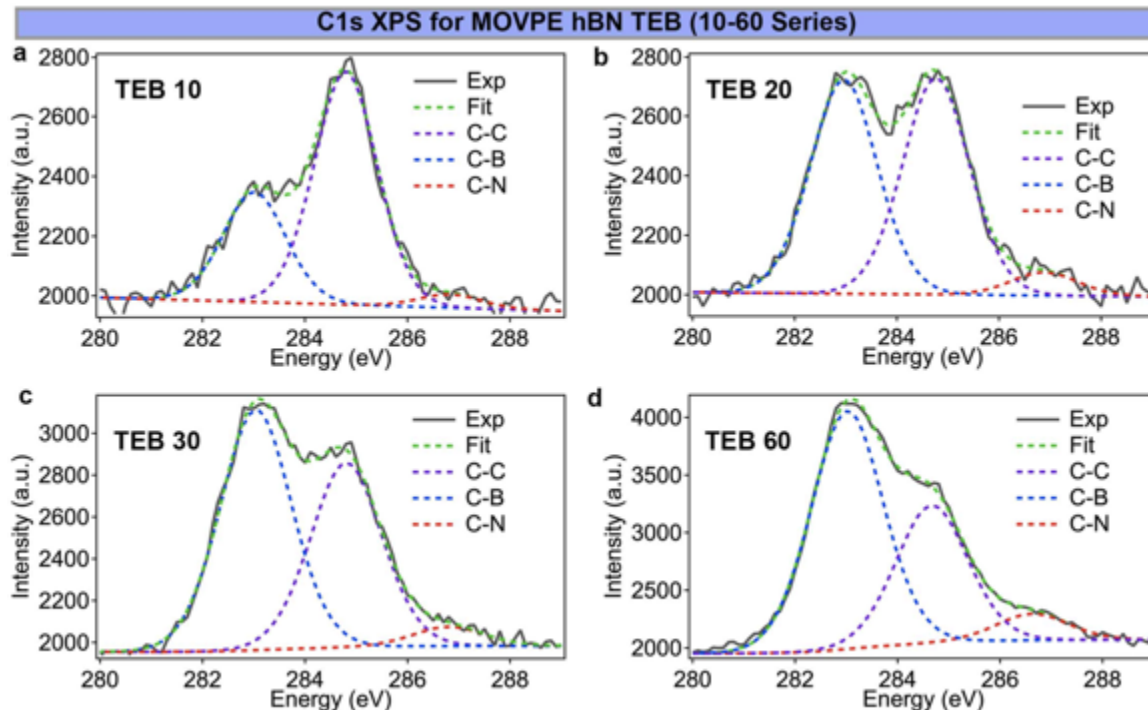

Figure S3—XPS C1s Spectra from MOVPE hBN TEB series- *MOVPE hBN samples with increasing TEB flow.* ***a.*** *MOVPE hBN (TEB 10).* ***b.*** *MOVPE hBN (TEB 20).* ***c.*** *MOVPE hBN (TEB 30).* ***d.*** *MOVPE hBN (TEB 60).*

X-ray photoelectron spectroscopy (XPS) was performed to estimate the levels of carbon incorporated in the hBN films during MOVPE growth. A gentle Ar beam was used to etch the hBN material, removing adventitious carbon from the surface. This surface carbon appears in the XPS spectra as C-C bonding. The measurement was performed on bulk samples with ~40 nm thickness prior to Ar etching.

Figure S3 displays the C1s XPS data collected from the MOVPE hBN samples with varying TEB flow rates. This data was previously published where further experimental details can be found,[3] however, for this work we additionally characterized the percentage of C-N bonding in the resulting hBN films. There are three primary peaks occurring the C1s portion of the spectra:

1. The peak at ~283.0eV is attributed to C-B bonds.[3, 4]
2. The peak at ~284.4eV is attributed to C-C bonds. [3, 4]
3. The peak at ~285.5eV is attributed to N-C bonds. [3, 5, 6]

Adventitious surface carbon appears in the XPS spectra as C-C bonding. Importantly, the rate of C-C bonding remains approximately consistent across the samples, suggesting that the C-C contribution is the result of adventitious carbon sources, and not incorporated within the hBN material itself. The B-C and N-C bonding contributions are attributed to bonding within the hBN itself. Both B-C and B-N bonding increase with TEB flow.

The reason for the much higher value of B-C bonding relative to N-C bonding is attributed to preexisting B-C bonds in the boron precursor, and the nature of the flow modulation growth.[3] Meaning that during hBN growth, the precursors –triethyl borane (TEB) and ammonia (NH3)— are not pushed into the reactor chamber simultaneously. They are introduced as short alternating pulses. TEB pulse is 1 sec and NH3 pulse if 3 sec. Accordingly, when TEB is pulsed, there is no ammonia flow, so boron atoms will occupy hBN lattice sites. During the NH_3 pulses the majority of the carbon containing ethyl groups are removed as volatile impurities, but a small fraction of carbon can also be incorporated into hBN as an impurity. As TEB flow rate increases, the volatilization of carbon is not completed during the ammonia pulse sequence, and more carbon is incorporated into the hBN lattice directly.
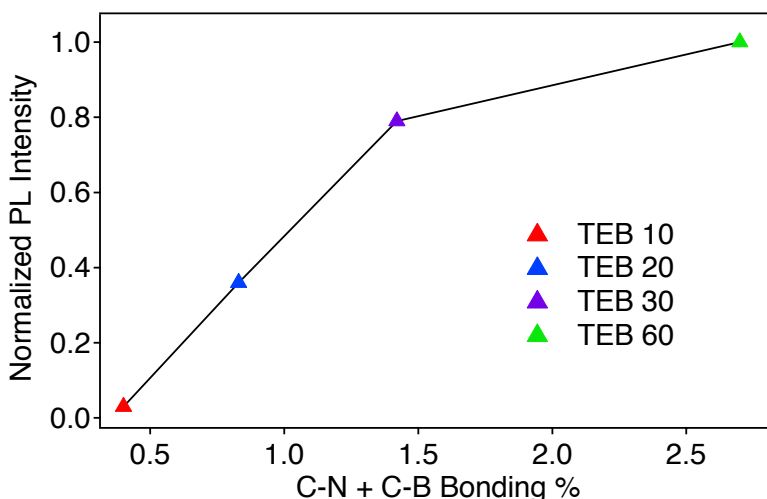
Figure S4—PL intensity of MOVPE hBN with increasing TEB flow vs the B-C+B-N Bonding %. *The integrated intensity of the ZPL peak from each MOVPE sample (as plotted in Figure 1a) is plotted against the bonding percentage of C-B + C-N as determined by XPS. For TEB 10,20,30 we see an almost perfectly linear trend. For TEB 60 we observe a slightly reduced intensity increase, likely the result of non-radiative decay pathways induced by an increasingly defective material.*

Quantifying the relative percentages of B-C and B-N bonding for the series of MOVPE films additionally permits a direct comparison of the measured carbon content (B-C + N-C bonds) to the observed fluorescence intensity from carbon ensembles. Figure S4 shows the average intensity of ensemble emission vs. the combined percentage of C-B and C-N bonding, confirming a near perfectly linear trend for TEB 10, 20, 30. We attribute the slight deviation from this trend (i.e. a decrease in PL signal) observed for the TEB 60 sample to increased disorder in the material—which has been reported to quench photoemission from SPEs due to non-radiative decay pathways.[7] It should be noted that previous structural analysis of hBN samples synthesized with increasing TEB flow rates concluded that the layered nature of the material is preserved, which confirms the material is C-doped hBN rather than a hybrid BNC material.[3]

d. Room Temperature ODMR from SPE ensembles in MOVPE (TEB 60)

In order to determine the g_e value of ODMR resonance observed, yet without knowledge of the spin state or nuclear coupling of the observed ODMR resonance, we fit the data with the generalized equation:

$$\Delta E = \mu_B * g * B \qquad \text{(Equation S1)}$$

Where E is the observed ODMR resonance frequency, μ_B is the Bohr magneton, and B is the applied magnetic field.

Figure 1D displays the observed ODMR contrast as a function of the resonant frequency when varying the external magnetic field. Figure S5 plots the observed resonant frequencies as function of the applied magnetic field. To extract the value for g_e, we fit the data with equation S1, extracting a g_e value of 2.09.
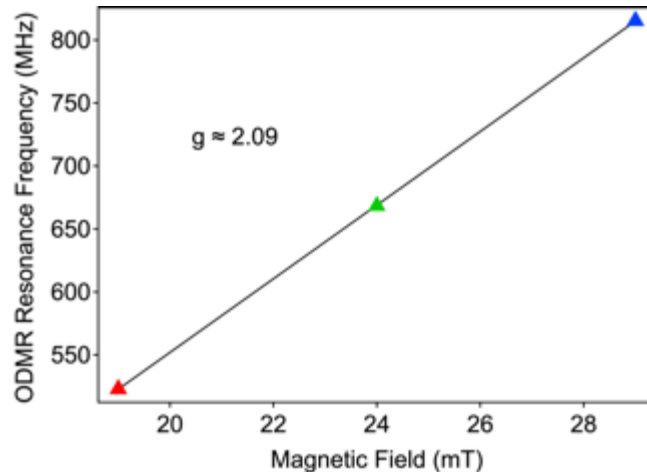
Figure S5—Extraction of g value from room temperature ODMR (TEB 60). *ODMR resonance frequencies as a function of applied magnetic field, extracted from figure 1e. The data points are fit with equation S1 and yield an extracted g value of ~ 2.09.*

We did not observe a zero-field splitting, evidence of a second transition frequency, or hyperfine splitting in our measurements. As a result, these results do not allow us to be conclusive about the

multiplicity of the spin sublevels we are probing, as our observation may be consistent with either a S=½ or S≥½ system with a small ground state splitting.

When comparing our room-temperature ODMR results from ensembles emitting at ~580 nm to that recently found at low temperature for a single or few peaks with a primary ZPL at ~727 nm, we find remarkable similarities.[8] Both display a single resonant peak again consistent with either a S=½ or S≥½ system with a small zero-field splitting. The peak width is narrow, as low as ~30–35 MHz, and a lack of observed hyperfine splitting. These similarities may point to a single structural origin of the visible region SPE emission which ranges from ~550-800 nm.

Finally, we investigated the temperature dependence of the OMDR resonance from the MOVPE (TEB 60) sample to investigate if the FWHM of the resonance is decreased with temperature. In some color centers like the silicon vacancy in silicon carbide the ODMR linewidth decreases with temperature because the linewidth of the resonance can be fully described given the spin coherence time of the defect, which increases with decreasing temperature.[9] In such a case the linewidth is the inverse to the coherence time. Figure S6 displays the temperature dependence of the ODMR resonance observed in our sample, where no narrowing of the resonance is observed upon cooling. This observation is important, suggesting that the resonance is not governed simply by the coherence time. As mentioned in the previous demonstration of ODMR from hBN SPEs in the visible region, [8] a D value within the line width is likely, and if it could be resolved it would display a temperature dependent behavior. As a result, the most likely broadening mechanism at play is the dipole-dipole coupling, i.e. by hyperfine interactions with nearby nuclei.
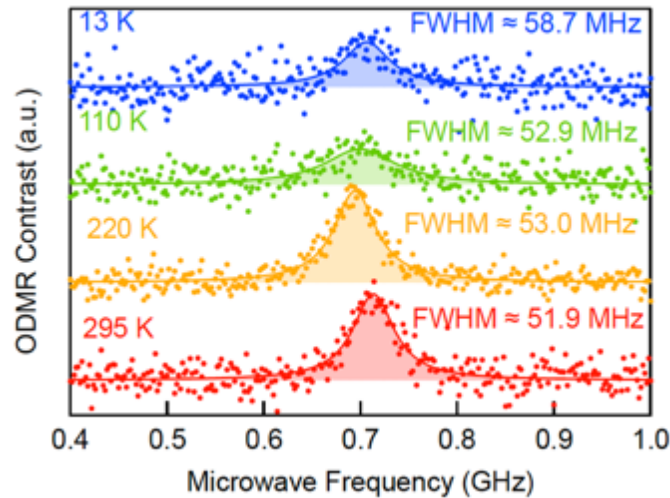
Figure S6—Temperature dependent ODMR of MOVPE (TEB 60) hBN. We recorded the ODMR contrast from the highly carbon doped MOVPE (TEB 60) sample at four temperatures between 295-13 K. A similar FWHM of the resonance suggests the broadening is dominated by unresolved hyperfine interactions.

e. Emission energies of incorporated SPE zero-phonon lines in MOVPE and MBE samples

Figure S7 displays histograms plotting the observed ZPL positions from single photon emitters in a variety of epitaxially grown hBN samples. Figure S7a displays the ZPL histogram for the MOVPE hBN (TEB 10) sample where SPEs are clustered around 585 nm. Specifically, ~78% of the emitters are located at (585 ± 10) nm, and 95% at wavelengths < 600 nm. This histogram is

reminiscent to that observed previously from CVD hBN grown on copper using ammonia borane as a precursor, reproduced in Figure S7b from ref [S10].[10] Such a clustering of emission lines in this region has also been reported for CVD hBN grown on platinum foil using a borazine precursor.[11] As a result we can classify the clustering of emission lines near 585 nm as an emergent feature during bottom up growth of hBN despite using different growth techniques, precursors, and growth surfaces. Further understanding of this phenomenon would greatly aid the deterministic fabrication hBN SPEs during growth.
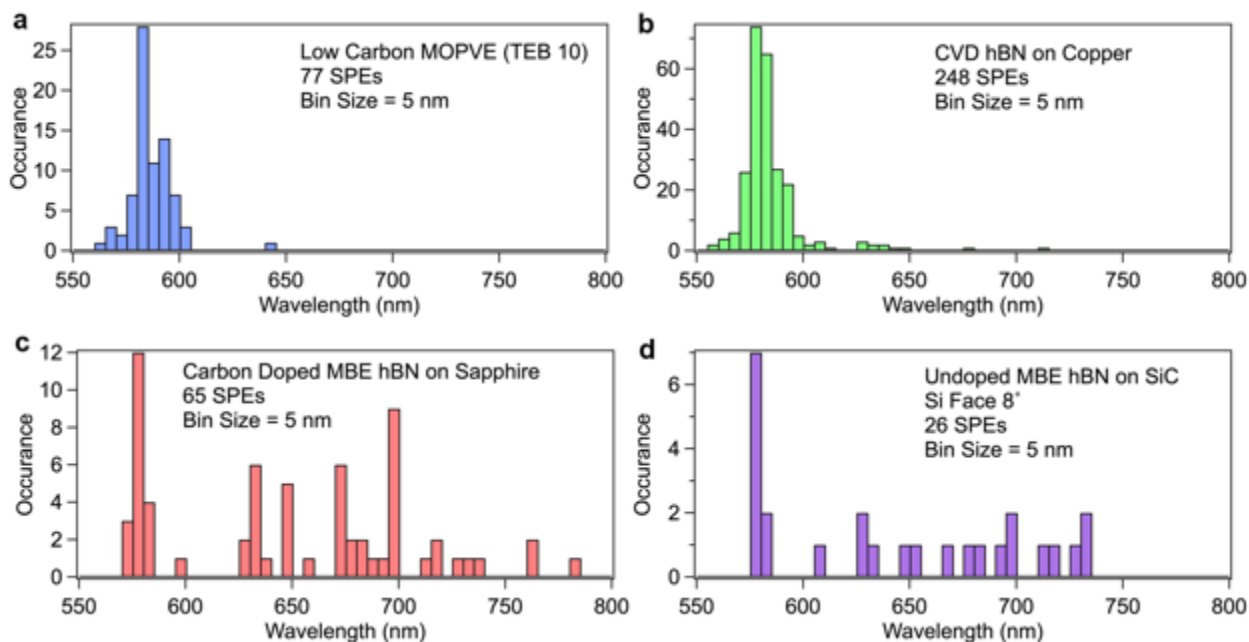
***Figure S7—Histograms of ZPL positions from various epitaxial sources. a.** 77 SPEs characterized in MOVPE hBN (TEB 10) display ZPLs clustered around 585±10 nm. **b.** 248 SPEs characterized from CVD hBN on copper display ZPLs clustered around 580±10 nm, reproduced from ref S9. **c.** 65 SPEs characterized in carbon doped MBE hBN on sapphire display ZPLs ranging across the visible spectrum. **d.** 26 SPEs characterized in undoped MBE hBN on silicon carbide displaying ZPLs ranging across the visible spectrum.*

Additionally, we recorded the ZPL locations of 65 different emitters from the carbon doped MBE hBN on sapphire, Figure S7c. The ZPL wavelength spectral distribution of the samples grown by MBE is approximately ~31% <600 nm, ~55% in the 600–700 nm range, and ~14% >700 nm. This lies in stark contrast to the ZPLs observed in the CVD and MOVPE samples discussed above and for which ~95% of the ZPL wavelengths is <600 nm. A possible explanation is that in the MOVPE sample only one type of carbon-based defect is formed while in the MBE sample different defects do form. Critically, the observation of the extended energy range of ZPL occurrences in the MBE sample (appearing only in the presence of carbon) hints that the entire range of visible SPEs may be due to carbon-related defects: either multiple defects (e.g. carbon-related complexes) or a single structural defect with variations in the ZPL energy due to local strain and Stark effects.[12, 13] Regardless of the interpretation of one or many defects, detailed comparison of the material properties of carbon doped MBE films to that of MOVPE or CVD films, may shed light on what dictates the natural occurrences of ZPL positions during bottom up growth.

Figure S7d shows the distribution of 26 ZPL wavelengths from the MBE hBN on SiC (Si 8°) sample. Similar to the carbon doped MBE on sapphire we found that the ZPL positions were evenly

distributed across the visible range: 35% <600 nm, 46% in the range 600–700 nm, and 19% >700 nm. We note that the similarity in ZPL energy distributions between the MBE sample types, occur despite different growth surfaces, boron precursor sources, and substrate temperatures.

Supplementary Information II: Additional Characterization of Implanted hBN Samples

a. Sample thickness of implanted hBN samples

Figure S8 displays the AFM scan of an MOVPE hBN (TEB 10) sample transferred from sapphire to SiO_2. The sample displays a thickness of ~40 nm, or roughly 120 monolayers of hBN. MOVPE hBN (TEB 10) samples from the same growth run were used for the implantation experiments of various ion species.
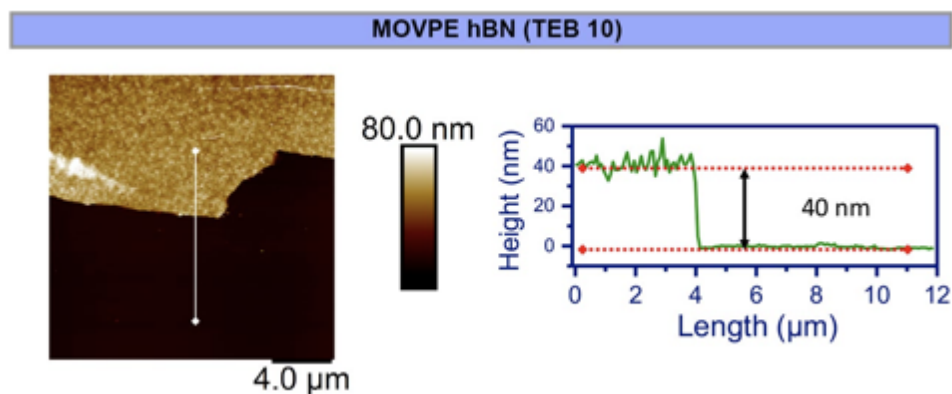
Figure S8—AFM on MOVPE hBN (TEB 10) sample used for implantation experiments. *A MOVPE hBN (TEB 10) film was transferred to SiO_2 and scanned by AFM to determine the sample thickness. The height trace shown to the right was taken from the white line showing a sample thickness of ~40 nm.*

b. Additional data from carbon implanted hBN samples

We performed carbon ion implantation experiments on two different types of hBN, MOVPE (TEB 10) and exfoliated bulk hBN crystals (Graphene Supermarket). For each hBN type, carbon was implanted at a series of doses ranging from $1*10^{11}$ to $1*10^{14}$ ions/cm^2, and subsequently analyzed through two primary methods, first confocal PL allowing us to collect the spectrum from localized spots of the sample, and second, wide-field imaging which allowed for semi-quantitative analysis of the defect density upon ion implantation.

Figure S9 shows the wide field images taken from MOVPE hBN implanted with carbon at doses from $1*10^{11}$ to $1*10^{14}$ ions/cm^2 before and after annealing the samples at high temperature. Equivalent to that displayed for exfoliated hBN flakes in Figure 4a. Figure S9b shows an identical implantation series after high temperature annealing. There is a clear increase in the density of SPEs which scales directly with the implanted carbon dose.
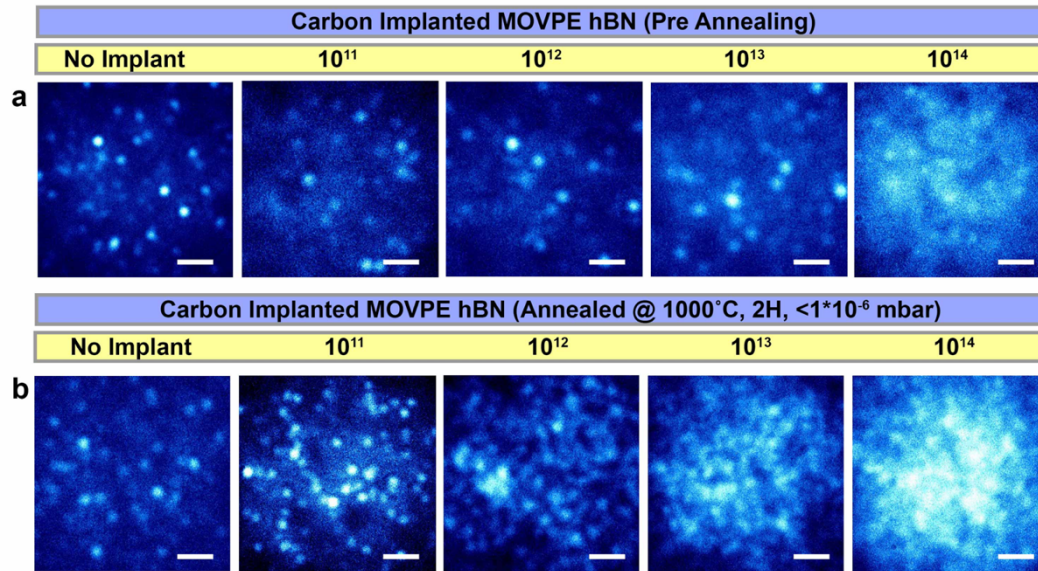
Figure S9—Wide-field imaging of MOVPE hBN carbon implanted dose series. *The scale bar in each is 2 μm.* **a.** *Un-implanted MOVPE hBN reference sample and carbon implanted samples with varying fluence of $1*10^{11}$-10^{14}.* **b.** *The same set of samples after high temperature annealing.*

Figure S10— Wide-field imaging and spectral analysis of MOVPE hBN implanted with carbon.
The scale bar in each is 2 μm. ***a.*** *Un-implanted MOVPE hBN reference sample.* ***b.*** *MOVPE hBN implanted with carbon at a fluence of $1*10^{11}$ ions/cm².* ***c.*** *MOVPE hBN implanted with carbon at a fluence of $1*10^{12}$ ions/cm².* ***d.*** *MOVPE hBN implanted with carbon at a fluence of $1*10^{13}$ ions/cm².* ***e.*** *MOVPE hBN implanted with carbon at a fluence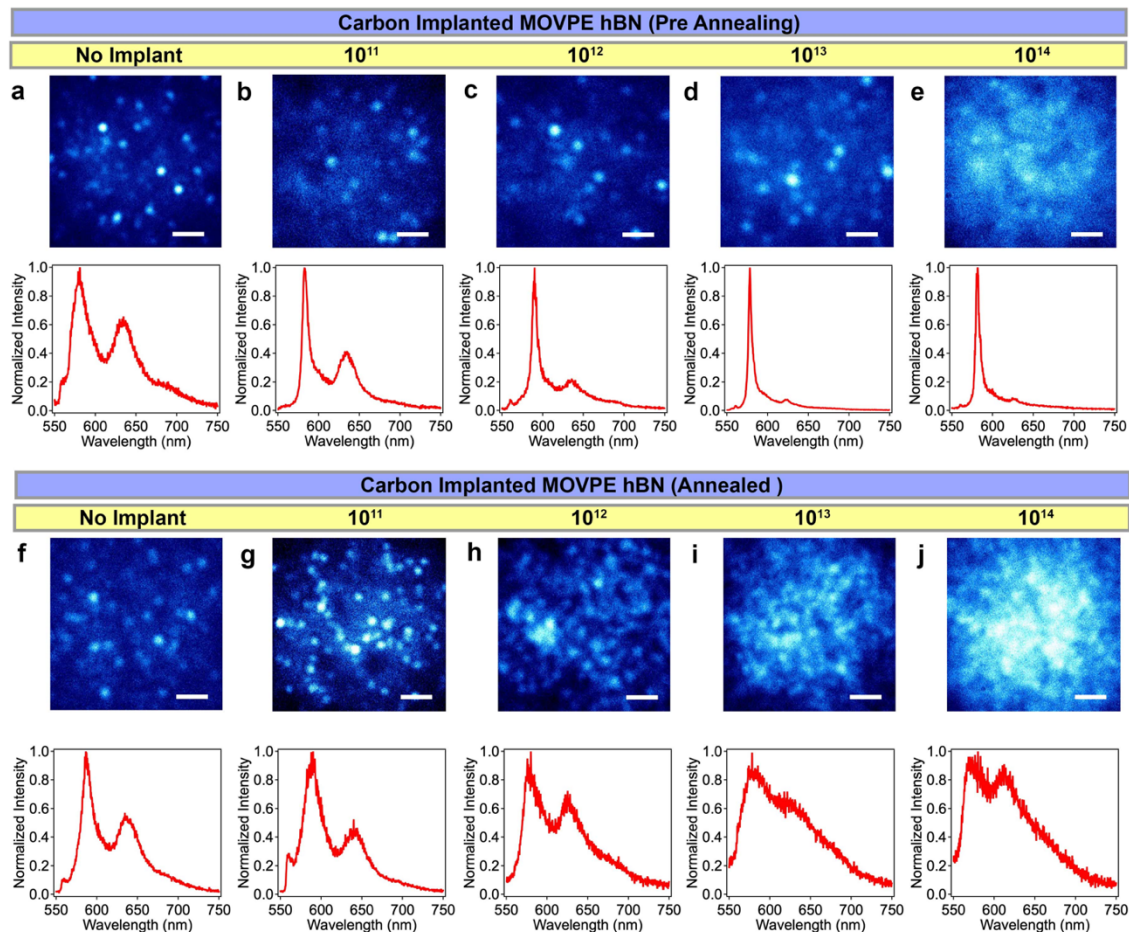 of $1*10^{14}$ ions/cm². f-j samples were annealed at 1000˚C for 2 hours under vacuum ($<1*10^{6}$ mbar).* ***f.*** *Un-implanted MOVPE hBN reference sample.* ***g.*** *MOVPE hBN implanted with carbon at a fluence of $1*10^{11}$ ions/cm².* ***h.*** *MOVPE hBN implanted with carbon at a fluence of $1*10^{12}$ ions/cm².* ***i.*** *MOVPE hBN implanted with carbon at a fluence of $1*10^{13}$ ions/cm².* ***j.*** *MOVPE hBN implanted with carbon at a fluence of $1*10^{14}$ ions/cm².*

Figure S10 shows the same set of widefield images for MOVPE hBN implanted with carbon as in Figure S9, however, while also displaying a typical spectrum for the implanted samples. Figure S10a shows the un-implanted reference sample, in which present emitters tend to show very broad ZPL lines, and strong coupling to the LO_1&LO_2 phonon modes as is typical from MOVPE SPEs which are created during growth. Figure S10b-e displays a representative spectrum located for the implanted samples at varying carbon fluences. In each case they display noticeably sharper ZPLs, which are attributed to those created during the implantation, similar to Figure 3b. Figure S10f-j displays the wide field images corresponding to the carbon implantation dose series of MOVPE (TEB 10) hBN after high temperature annealing (1000˚C, 2 hours, $<1*10^{-6}$ mbar) with the associated representative spectrum in each case. Predominantly sharp emission lines give way to SPEs showing a much stronger coupling to bulk LO phonon modes. As the implantation dose increases the isolated emission centers apparent in the wide field transition to a much denser emission pattern, and the associated spectra for each can be seen to similarly transition from single isolated SPEs to an ensemble of a few SPEs per laser spot.

Next we analyzed the typical spectra associated with the wide field images displayed in Figure 4 for high-purity exfoliated hBN. Figure S11 displays a representative spectrum observed from each respective implantation fluence corresponding to the associated wide field image. For the un-implanted sample, we were unable to locate any SPEs in the confocal scan, and the spectrum in Figure S11a shows a typical weak background emission as well as the clearly resolvable hBN Raman peak, shown here centered at ~574 nm (as expected for 532 nm excitation). Figure S11b-e display similarly representative spectra from each sample. Similar to the SPEs characterized upon carbon implantation of MOVPE prior to implantation we observe sharp ZPL lines in each, and very little coupling to LO phonon modes. The observation of these sharp ZPL lines upon carbon implantation of multiple material types supports our hypothesis that these defects are those created during implantation. Figure S11f-j displays the typical spectrum observed post annealing. We see very few bright defects created in the flat regions of the exfoliated flake upon annealing. The associated spectrum again displays the hBN Raman signature at ~574 nm, as well as the Raman signal from the underlying Si substrate. Figure S11g-j displays the carbon implanted samples with increasing dose post-annealing. In each case, we find localized SPEs showing typically broad emission lines and increased phonon coupling compared to their pre-anneal counterparts, similar to that observed for implantation into the MOVPE samples.
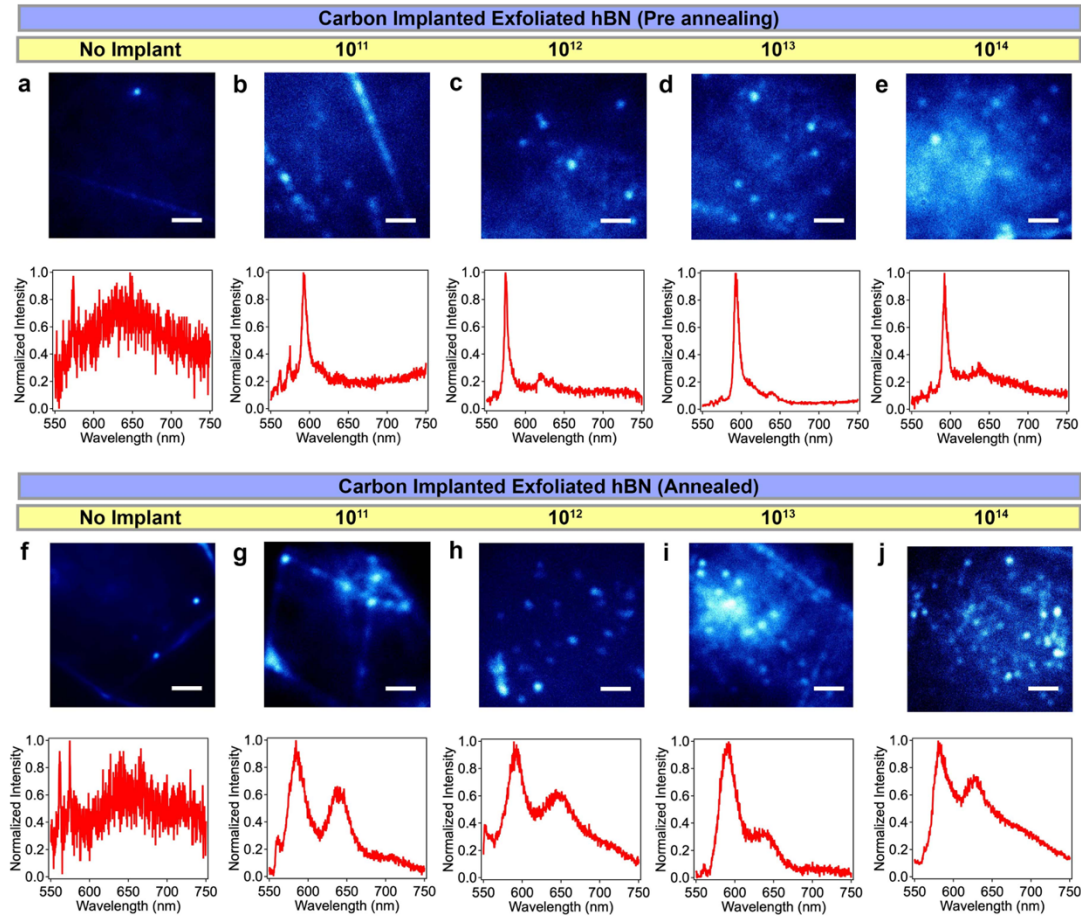
Figure S11— Wide-field imaging and spectral analysis of exfoliated hBN implanted with carbon prior to annealing. *The scale bar in each is 2 μm.* ***a.*** *Un-implanted exfoliated hBN reference sample.* ***b.*** *Exfoliated hBN implanted with carbon at a fluence of $1*10^{11}ions/cm^2$.* ***c.*** *Exfoliated hBN implanted with carbon at a fluence of $1*10^{12}ions/cm^2$.* ***d.*** *Exfoliated hBN implanted with carbon at a fluence of $1*10^{13}ions/cm^2$.* ***e.*** *Exfoliated hBN implanted with carbon at a fluence of $1*10^{14}ions/cm^2$. f-j samples were annealed at 1000˚C for 2 hours under vacuum ($<1*10^6 mbar$).* ***f.*** *Un-implanted MOVPE hBN reference sample.* ***g.*** *MOVPE hBN implanted with carbon at a fluence of $1*10^{11}ions/cm^2$.* ***h.*** *MOVPE hBN implanted with carbon at a fluence of $1*10^{12}ions/cm^2$.* ***i.*** *MOVPE hBN implanted with carbon at a fluence of $1*10^{13}ions/cm^2$.* ***j.*** *MOVPE hBN implanted with carbon at a fluence of $1*10^{14}ions/cm^2$.*

c. Analysis of SPEs created by carbon implantation

As discussed in the manuscript, carbon implantation into the MOVPE display extremely narrow emission lines from ~575-590 nm, displaying $g^2(0)$ values <0.5. This feature was also observed in carbon implantation experiments into exfoliated hBN flakes; however, we will restrict our discussion in this section to those emitters created and characterized in carbon implanted MOVPE hBN. The findings are intriguing as the emission lines occur in roughly the same position as the typical ZPL for SPE created during growth. However, what significantly differentiates these

SPEs, is they display extremely narrow emission lines, with very little coupling to longitudinal optical (LO) phonon modes.

Figure S12 displays twelve selected SPEs from as-grown MOVPE hBN (TEB 10), shown in blue, and from carbon implanted MOVPE hBN (TEB 10) prior to annealing, shown in red. As it can be seen the linewidth, represented as the FWHM of the single Lorentzian ZPL fit, is significantly reduced for the emitters created *via* ion implantation. These emitters display a ZPL linewidth of ~5 nm on average, and a minimum of ~2.5 nm. Conversely, those found in the as-grown samples show a minimum FWHM of ~8 nm and an average value of ~20 nm, or nearly 4-fold broader on average. We also note while the comparison is made for only 12 emitters each, of 77 analyzed SPEs in the as grown sample, the FWHM of ~8 nm is the lowest measured. The variation in the linewidth, as well as the lack of LO coupling allow us to confidently assert that these particular emitters are those created *via* the ion implantation process.
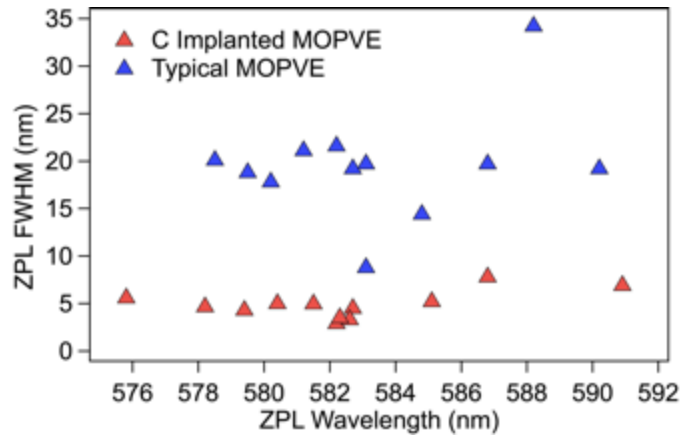
Figure S12—ZPL FWHM comparison of SPEs located inside the C implanted region to as-grown single photon emitters in MOVPE hBN (TEB 10). *Blue triangles correspond to SPEs analyzed from as-grown MOVPE hBN (TEB 10). Red triangles correspond to SPEs located within the C implanted region of the same sample.*

To analyze in further detail the spectrum of these emitters, we selected the emitter displayed in Figure 3b with a mint green color. Figure S13a displays the spectrum for this particular emitter. Figure S13b displays the corresponding 3 Lorentzian fits utilized corresponding to the ZPL in green, the low energy longitudinal acoustic (LA) phonons in purple, and the LO phonons in pink. hBN SPEs are known to couple strongly to 2 LA modes and 2 LO modes,[1, 2] however, each phonon subset is only modelled by a single Lorentzian in our analysis as the separate modes are not resolved. Comparing the integrated peak intensities, we are able to roughly evaluate that ~57% of the photons are emitted through the ZPL, ~37% are emitted the low energy LA phonon sidebands, and only ~6% are emitted through the LO phonon modes. Figure S13c displays a zoomed region around the ZPL, a demonstrating the good fit to experiment obtained by modelling only a single LA mode. From this we can extract a ZPL centroid position of 578.1 nm and a FWHM of 3.5 nm.
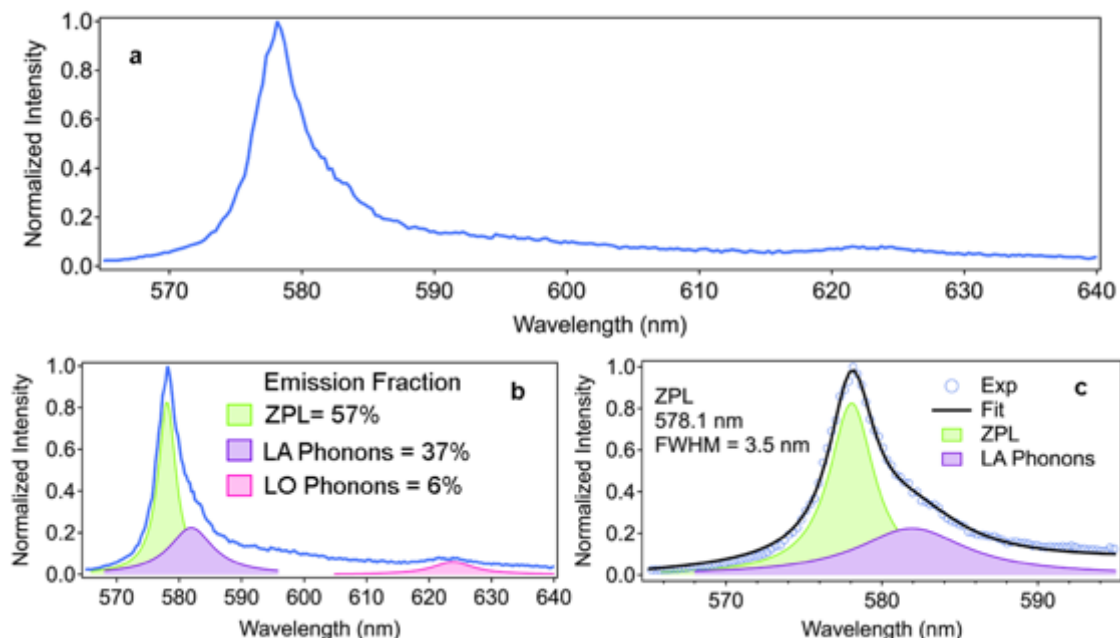
Figure S13—Narrow SPE created by C implantation. a. *Spectrum of narrow SPE created by carbon implantation.* ***b.*** *3 single Lorentzian fits modelling the ZPL, coupling to low energy LA phonons, and coupling to LO phonon modes.* ***c.*** *Zoomed region of the ZPL and LA phonon modes, and the corresponding fit to the experimental signal.*

While it is not uncommon to observe relatively narrower ZPL lines and lower phonon coupling for visible region hBN SPEs with energy transitions <1.8 eV (~689 nm), it is far less common to observe such features for emission around 2.1eV as we see here.[14] Furthermore, epitaxially grown hBN is typically of lower material quality than exfoliated flakes and has been shown to display broadened linewidths as a result. All of these features make the narrow line shape of these centers very easy to distinguish, making the conclusion that those SPEs with narrow lines are those created upon implantation a relatively straightforward. This interpretation is reinforced by the fact that these narrow lines are not observed for either Si or O implantation, meaning the lines are unlikely to arise from vacancy generation or the activation of pre-existing defect centers.

d. Silicon and Oxygen control implantations into MOVPE (TEB 10)

In addition to the carbon implantation detailed in Figure 3, we performed identical implantation experiments with oxygen and silicon. As with carbon implantation, for both Si and O the implanted regions display an increased intensity prior to annealing. Figure S14a displays the typical spectrum from the implanted region of the oxygen-irradiated samples, prior to annealing. Only two notable spectral features are observed, the silicon Raman line from the underlying substrate, and a broad peak spanning over the spectral range ~720–820 nm. Note that the peak artifacts above 800 nm are due to the optics used in our confocal setup which are optimized for the visible region. Recent work has identified this broad emission at ~820 nm as the negatively charged boron vacancy (V_B^-).[15] Importantly, the observation of the V_B^- emission spectra which is relatively strong and homogeneously distributed throughout the implanted region, confirms a high degree of vacancy creation upon implantation, consistent with our SRIM simulations, as shown in Figure S15. No

evidence of sharp emission lines similar to that from carbon implantation are found, and almost no SPEs were located within the 50-μm^2 area, suggesting that potentially pre-existing SPEs were largely destroyed by oxygen implantation.
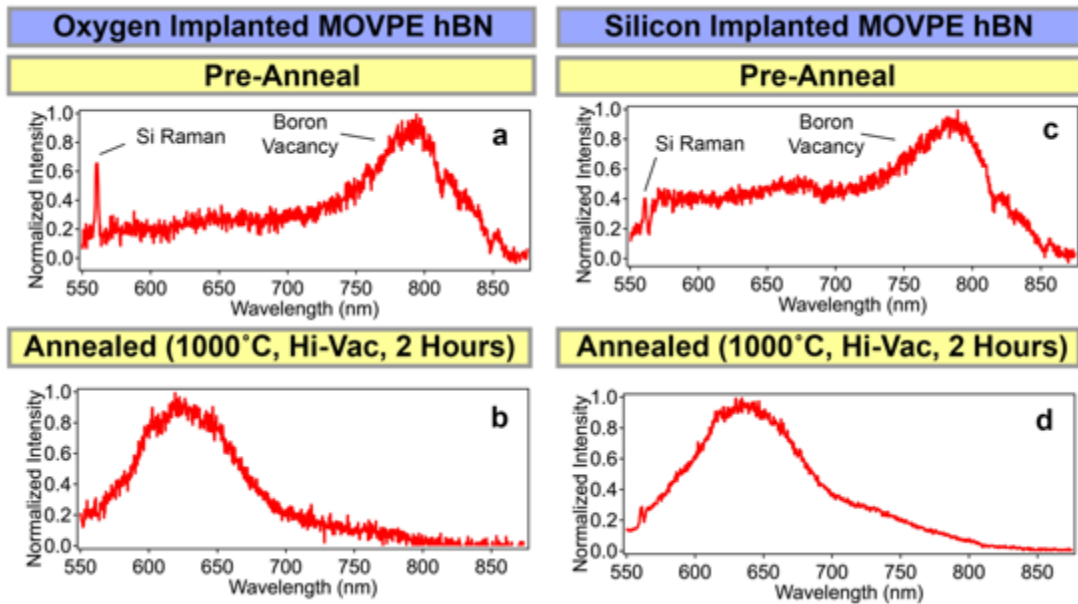
Figure S14—MOVPE hBN (TEB 10) Samples implanted with oxygen and silicon. *Implantations were done at a dose of 10^{13} ions/cm^2 and an energy of 10 keV, using a TEM grid with 50 μm^2 apertures as a mask. **a.** Typical spectra observed in the oxygen-implanted region pre-annealing, showing only background emission the V_B^- peak ~ 800 nm are observed. **b.** Characteristic spectrum from oxygen implanted region post annealing, with the only spectral signature observed is a broad peak at ~ 630 nm. **c.** Typical spectra observed in the silicon-implanted region pre-annealing, showing only background emission the V_B^- peak ~800 nm are observed. **d.** Characteristic spectrum from silicon implanted region post annealing, with the only spectral signature observed is a broad peak at ~ 630 nm.*

Figure S14b displays the typical spectrum observed from the oxygen implanted area after high temperature annealing. The implanted region displays a broad signal centered at ~630nm and shows no evidence of the ensemble emission at ~585 nm observed with high carbon doping during growths or carbon implantation. Additionally, the lack of a PSB or other features consistent with an ensemble of hBN SPEs allows us to exclude that this emission may originate from an ensemble of the carbon-based SPEs centered at ~630 nm. The silicon implanted MOVPE hBN (TEB 10) samples display nearly identical fluorescence properties within the implanted regions as the oxygen implanted samples. Figures S14c and S14d display the results for before and after annealing, with similar formation of (V_B^-) before annealing and broad emission in the visible spectral region after.

e. SRIM simulations for ion implantation results.

Figure S15, displays the Monte Carlo simulations utilizing the Stopping and Range of Ions in Matter (SRIM) software. We note that for interpreting these results, it is important to consider the utilized ion implantation dose of ~10^{13} is the equivalent of 1 incident ion/10nm^2 at the top hBN monolayer. For all plots the ion values are reported in concentration/cm^3. The simulations were run for 50,000 incident ions into hBN. Figure S15a displays the average stopping depth for each

implanted species, demonstrating that the relative doping concentration in a 40 nm film (400 Å) increases with the size of the implanted ions. While 100% of the implanted Si ions and ~93% of the implanted O ions stop within the 40 nm hBN film, only ~72% of the carbon atoms are stopped within the hBN film.
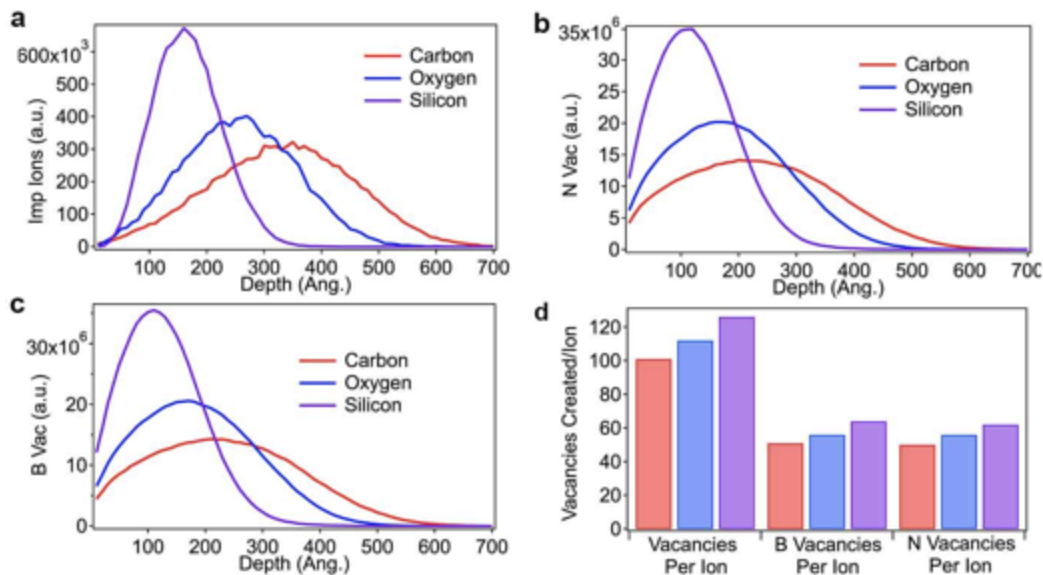
Figure S15—Monte Carlo Stopping and Range of Ions in Matter (SRIM) simulations of ion implantation experiments. All simulations were performed for 50,000 incident ions and the values reported are listed in ions/cm³. **a.** *Simulated average stopping depths of different ion species implanted into hBN.* **b.** *Simulated nitrogen vacancy creation by implantation depth for different ion species.* **c.** *Simulated boron vacancy creation by implantation depth for different ion species.* **d.** *A plot of total vacancies, and B&N vacancies per incident ion for different ion species.*

Figure S15b&c display the simulated nitrogen and boron vacancy creation per incident ion. As expected from the average ion stopping depths, the vacancy creation of larger ions tends to take place at shallower depths than their lighter counterparts. Figure S15d displays the total vacancies and respective B and N vacancies per incident ion. It is clear that heavier ions create more vacancies. We finally note that the suggested vacancy creation simulations are based on an amorphous hBN material, and likely over exaggerate the actual vacancy creation. Despite this, the high degree of vacancy creation is confirmed by the observation of homogeneous boron vacancy creation as evidenced in Figure S14.

Supplementary Information III: Expanded discussion comparing experimental results with literature

a. $V_B C_N$- formation in implantation experiments

The identified $V_B C_N$- defect qualitatively matches our experimental findings well. Simulations suggest that only the boron-vacancy (V_B) is mobile under the annealing conditions (1000˚C), while divacancies are not mobile under 1400˚C, and nitrogen vacancies are not mobile at any

temperatures below the hBN melting point.[16] Furthermore, above 840°C V_B defects are believed to mobilize and trap at nearby nitrogen vacancies, creating stable divacancies.[16]

This is consistent with a number of our experimental observations. First, the decay of V_B-fluorescence upon annealing, suggests migration of V_B-. Second the subsequent appearance of SPE ensembles in the carbon implanted samples. Carbon interstitial atoms, likely to be abundant after implantation, are thought to be mobile between ~310-360K.[17] In which case there are two potential mechanisms for V_BC_N- formation. First, V_B- centers created *via* ion implantation are mobile upon annealing, where some portion of these centers is then trapped at C_N centers, creating a V_BC_N defect complex. Second, that created or preexisting stable divacancies trap preexisting carbon atoms upon annealing.

b. Previous literature on hBN SPE creation

Considering our results on the creation of carbon-based defects by multiple methods, we deem important commenting on previous reports in the literature aimed at deliberately creating emitters in hBN. A number of methods have been employed: high temperature annealing,[14, 18] plasma treatment,[19] strain activation,[20] electron beam irradiation,[14, 21] ion implantation (although never involving carbon),[22] and focused ion beam (FIB) irradiation.[23] The results from these experiments have been largely inconclusive and, at times, conflicting. Considered in their entirety, previous results largely suggest that preexisting emitters are activated rather than created in hBN.[18] This is plausible as even the highest quality hBN material, grown by HPHT precipitation, is known to incorporate carbon.[24]

c. Bowl shaped distortions of V_BC_N- as an explanation for observed range of observed photophysical properties

Intriguingly, while the $V_BC_N^-$ was selected purely based on the 3 experimental filters, an interesting feature described in detail later is that single-layer models of the emitting state are predicted to undergo a small out-of-plane distortion. The nature of this distortion is found to be environment and calculation-method sensitive, with some calculations of 3-layer models indicating complete loss of the distortion and others predicting that it leads to large bowl-like structures, as are known for graphene layers. This sensitivity to environment offer a plausible explanation to the well-known variation in emission properties of visible defects such as ZPL energy[14, 25] and phonon coupling.[1] Furthermore, the predicted high sensitivity to both local electric and strain fields, not common for other known point defects in hBN,[15, 26] potentially explains the prevalence of spectral diffusion[27, 28] and large tuning magnitudes[12, 29] well documented for SPEs in the visible region.

Supplementary Information IV: Computational Modelling

a. Interpretation of experimental spectra in terms of readily calculable properties

The defects are excited at 532 nm, corresponding to an energy of 2.33 eV and a wavenumber of 18800 cm^{-1}. The most intense emission band is observed at ca. 580 nm (2.13 eV, 17200 cm^{-1})

and hence the maximum amount of energy that can be dissipated by non-radiative processes is 0.20 eV (1560 cm^{-1}). Such a small value makes it unlikely that the emission could occur by intersystem crossing between spin manifolds. The emission is also recognized as being very bright, with analogous emission previously quantified to have a high quantum efficiency > 60%[30] and a lifetime of ~2-6 ns.[31] Such results could only possibly be consistent with a large oscillator strength not much less than 1. Such a large oscillator strength and the small energy difference between absorption and emission make it highly improbable that the emission at 580 nm arises from a false origin associated with the Herzberg-Teller effect,[32] and hence the observed origin is assigned as the ZPL, giving the energy of the ZPL as $\Delta E_{00} = 2.13$ eV. Note that in this analysis, the effect of the acoustic phonons is incorporated into the ZPL width.

Quantification of the observed spectral widths is possible through the evaluation of the reorganization energy associated with excitation of optical phonons as a result of the photoemission:[33]

$$\lambda^E = \Delta E_{00} - h\frac{\int_0^\infty E(v)/v^2 dv}{\int_0^\infty E(v)/v^3 dv}$$

where $E(v)/v^3$ is the spectral bandshape function[34] and $E(v)$ is the emission intensity when the spectrum is scanned linear in frequency. As the observed spectra were scanned linear in wavelength as $E(\lambda)$, the conversion $E(v)/v^3 = E(\lambda)/v^5 \propto \lambda^5 E(\lambda)$ must also be applied. As a result of these effects, the raw spectra presented in the main text Figs. 1-3 significantly distort the intrinsic defect spectral properties, modifying properties such as the perceived spectral width. In addition, we modify the raw recorded spectra to account for the manufacturer's published calibration data for the photodetector and grating used. After smoothing to a Gaussian energy resolution of 0.01 eV, the resulting spectral bandshapes for an example emitter from both Region-I and Region-II are shown in Figure 5, from which ZPL energies ΔE_{00} and the emission reorganisation energy λ^E are determined. Results from multiple emitters are listed in Table S1. The similarity of the reorganization energies for Region-I and Region-II strongly support the interpretation that the both sets of spectra arise from the same defect, with the dramatic observed change in spectral lineshape arising as a consequence of some local variation. In Region I, low frequency changes in torsional and bending motions control linewidth, whereas in Region II changes in BN (or other) stretch coordinates dominate.

Table S1. Analysis of the ZPL band maximum ΔE_{00} and the reorganisation energy λ^E depicting the difference between this and the average emission energy for various emitters.

Region	E_{00} / eV	λ^E / eV
I (see Fig. 3b)	2.13	0.13
I	2.13	0.10
I	2.12	0.14
II (see Fig. 3c)	2.13	0.15
II	2.11	0.15
II	2.10	0.15

b. Electronic-structure computational methods

All calculations are performed on model compounds representing the defects containing either 3, 5 or 10 rings surrounding the central atom; in three-ring model compounds of V_BC_N and V_NC_B, an extra line of atoms is also added as this has been found to enhance convergence of calculations

with respect to sample size.[35, 36, 37] This approach avoids artefacts associated with inter-defect interactions present when 2D-periodic model systems are used, but at the expense of describing the boundary effects less well owing to the use of hydrogen termination. In terms of electronic structural properties, ringed model compounds converge quickly, with results for 1-ring models being generally descriptive and convergence attained at 3 rings.[35, 36, 37, 38] In terms of understanding the effects of acoustic phonons, the calculations converge slowly with respect to ring size, with 3-ring models being adequate for most purposes but 5-ring models needed for quantitative accuracy.[37] Calculations are also performed on a system containing three layers of the 10-ring model compound extracted from the hBN lattice containing 2171 atoms total. The spectral-simulation technology used can be applied to 30-ring 1-layer modes without great technical difficulty.

As a large number of defect states are considered for large models, most calculations are performed using density-functional theory (DFT), implemented amidst a mixed quantum-mechanics/molecular-mechanics (QM/MM) scheme for 10-ring models (see next subsection). DFT approaches can be very unreliable as traditional implementations poorly treat the static electron correlation effects that often dominate defect proeperties.[38] We use standard DFT solutions to the Kohn-Sham equations only to determine the ground state in each spin manifold considered. Within each manifold, excited states are then determined using time-dependent DFT (TDDFT) as this approach is numerically stable and less susceptible to systematic errors associated with open-shell character.[37, 38] The worst-case scenario for this approach is when the ground-state itself is highly open-shell in nature. For the defects considered herein, this applies in particular to the singlet manifold of V_NC_B.

An issue with DTDFT is that it may not represent double excitations well. Such excited states could arise if two electrons are transferred from one defect orbital to another, as is known to be relevant for V_NC_B and isoelectronic analogues. They present transitions that are formally forbidden, though weak intensity could arise through configuration interaction and/or Herzberg-Teller coupling. As we are searching for intense transitions that could account for observed optical processes, we do not perform an exhaustive search for this type of excited state.

Simplistic DFT functionals such as LDA and PBE underestimate band gaps and hence mostly give very poor results when applied to hBN defects. The mostly commonly used method in calculations has been the HSE06 hybrid functional,[39, 40] which corrects for this problem and is mostly stable. Nevertheless, it manifests an incorrect asymptotic potential and hence is subject to uncontrolled errors when applied to charge-transfer transitions, transitions than could manifest in defects.[41, 42, 43, 44] Also, when calibrated against high-level computational approaches on model systems, its results tend to be poor and associated maximum errors found are too large to make the method of general usefulness.[38]

Here, we mostly apply the CAM-B3LYP method.[45, 46] This is an asymptotically corrected hybrid density functional capable of treating charge-transfer transitions[41, 42, 43] and one of the few methods capable of giving generally useful results, including the details of highly resolved electron-phonon interactions, in extended aromatic chromophores akin to hBN like the chlorophylls.[47, 48, 49] For transitions in hBN defects with open-shell character no greater than that in the defects of current interest, its calculated excitation energies have been calibrated against high-level calculations and found to be within 0.5 eV, a seemingly large value but nevertheless one that is useful in the present context. CAM-B3LYP represents an entry-level method, an example of the simplest type of DFT approach not expected to be subject to uncontrolled errors for the scenarios of interest. Compared to *ab initio* approaches for defects, CAM-B3LYP tend to

underestimate transition energies,[38] something perhaps pertinent to the results that we present. For the most important problems, we also apply HSE06, an approach that usually underestimates transition energies more than does CAM-B3LYP.[38] Notably, we see no evidence of catastrophic failure of this approach for the cases considered. Also, we apply the *ab initio* method EOM-CCSD[50] to the most important problems, with this approach typically giving results closer to higher-level *ab initio* approaches than does CAM-B3LYP.[38]

All calculations on multi-layer models use the D3(BJ) dispersion correction.[51] Most calculations are performed using the 6-31G* basis set.[52] Test calculations using smaller and larger basis suggest that the results obtained are within ±0.1 eV of triple-zeta values.[36, 37] All calculations are performed using Gaussian16,[53] except some CCSD 2-ring model energies for V_NC_B calculated using MOLPRO.[54] Geometrical structures of particular interest, for both ground-states and excited states, are optimized using tight convergence criteria and shown to be local minima using vibrational analysis (no imaginary vibrational frequencies). Note, however, that some structures predicted to have a very small imaginary frequency as part of double-well potentials of depth less than 0.001 eV are reported as being of high symmetry.

Optimized coordinates for the most relevant structures, as well as the normal modes, Duschinsky matrices, and displacement vectors used in the simulation in Figure 5 are provided in Supporting Data.

c. QM/MM methodology

For the 10-ring model compound, some multi-layer systems, and some EOM-CCSD calculations, QM/MM calculations are performed using the ONIOM scheme.[55, 56] Mostly, the AMBER force field[57, 58] is used for the MM part. The intramolecular parameters in this force field were determined by fitting the geometry and vibrational density of states (DOS) calculated by CAM-B3LYP for a 5-ring model of a single hBN layer. The intermolecular van der Waals contributions were obtained by fitting to results for a 3-ring 3-layer hBN model optimized using CAM-B3LYP combined with Goerigk and Grimme's D3(BJ) dispersion correction.[51] Force-field contributions for impurity atoms such as carbon cancel during the QM/MM procedure and hence are not explicitly determined. A modified form of sp^2-hybridised carbon is used for both the carbon and boron parameters in the force field. Coulomb interactions involving atomic charges are not used in the force field as the net Coulomb interaction is small (less than 5% of the van der Waals term) yet arises from the near complete cancellation of large contributions that are sensitive to treatment of dielectric effects. While improved force fields with more general utility in describing intermolecular interactions could be derived, the current one serves the purpose of providing a description of the outer rings that is highly compatible with the CAM-B3LYP calculations used for the defect center. Only 2 rings are used when CAM-B3LYP is applied in the QM part of a calculation, though technically this would be easy to increase to five. This is because the number of rings used is found to have only a minor impact on the electronic properties of the defects of interest. When EOM-CCSD is used for the high-level method, either one or two rings are so treated, with the other rings treated using either TD-CAM-B3LYP or else the AMBER force field.

The AMBER parameters are specified to Gaussian-16 using the command "AMBER=SOFTFIRST" and the data:

HrmStr1   CA NC 280. 1.443
HrmStr1   CA CA 280. 1.443

```
HrmStr1   CA HA 281. 1.195
HrmStr1   NC HA 524. 1.01
HrmBnd1   CA NC CA 55. 120.
HrmBnd1   NC CA NC 55. 120.
HrmBnd1   CA NC HA 33. 120.
HrmBnd1   NC CA HA 33. 120.
HrmBnd1   CA CA NC 55. 120.
AmbTrs    NC CA NC CA 0 180 0 0   0.0 10.0 0.0 0.0  -1.0
AmbTrs    HA CA NC CA 0 180 0 0   0.0  9.0 0.0 0.0  -1.0
AmbTrs    NC CA NC HA 0 180 0 0   0.0  9.0 0.0 0.0  -1.0
AmbTrs    *  CA CA *  0 180 0 0   0.0  9.0 0.0 0.0  -1.0
VDW       CA 1.9000 0.141
VDW       NC 1.8240 0.17
VDW       HA 1.0000 0.0200
```

using the MM atom types "C-CA-0.0", "B-CA-0.0", "N-NC-0.0" and "H-HA-0.0" for carbon, boron, nitrogen, and hydrogen atoms, respectively. This data specifies the force constants. This is interpreted as:

HrmStr1- harmonic stretch between 2 atom types, defined by a force constant in kcal/mol $Å^{-2}$ and an equilibrium bond length, in Å.

HrmBnd1- harmonic bending between 3 atom types, defined by a force constant in kcal/mol per $radian^2$ and an equilibrium bond angle, in degrees.

AmbTrs- sinusoidal torsional potential with specified periodic angle, in degrees, and barrier height, in kcal/mol.

VDW- Lennard-Jones equilibrium distance contribution from each atom, in Å, and well depth contribution, in kcal/mol.

The default command line used to control Gaussian-16 for an excited state geometry optimization and normal-model calculation is:

#P   oniom(td(nstate=4,root=1)cam-b3lyp/6-31G*:amber=softfirst)   geom=connect opt(tight,maxstep=3,readfreeze,nomicro) freq

In addition, preliminary calculations were performed using external control of Gaussian-16 to utilize microiterations, with associated correction for the resulting loss of precise coordinate conservation and associated symmetry loss, whilst avoiding the need to use redundant internal coordinates for systems containing thousands of atoms.

The force field fits the CAM-B3LYP calculated BN bond length in a large cluster of 1.443 Å and the CAM-B3LYP/D3 calculated intermolecular layer separation of 3.33 Å. These values are also in good agreement with experimental data. Figure S16 shows the vibrational DOS as determined using CAM-B3LYP/6-31G* for a 5-ring model of h-HB, compared to the results from the AMBER force field that was fitted to it. The DOS is characterized by sharp features associated with N-H stretching at ~ 3625 cm^{-1}, B-H stretching at 2690 cm^{-1}, and B-N stretching at 1300 cm^{-1} (note that these results exceed observed values owing mostly to the neglect of anharmonicity in the calculation of the DOS). Broad bands associated with bending motions are found in the region 700 – 1600 cm^{-1}, whilst broad torsional bands are found in the region 0 – 1000 cm^{-1}.

A shortcoming of the force field is that it predicts that hBN model compounds of sufficient size are not flat but distort out of plane. Such an effect could be physically reasonable, and has been observed, e.g., for graphene monolayers, but there is no evidence to support the current predictions for hBN. In this work, care is therefore required when considering intrinsic out-of-

plane distortions associated with hBN defects. Also, the calculated interlayer binding energy from the CAM-B3LYP/D3 calculations is 0.202 eV per BN pair, much larger than the value of 0.040 eV obtained from quantum Monte-Carlo calculations,[59] but similar to values obtained using other DFT schemes embodying empirical corrections for dispersion.[59]
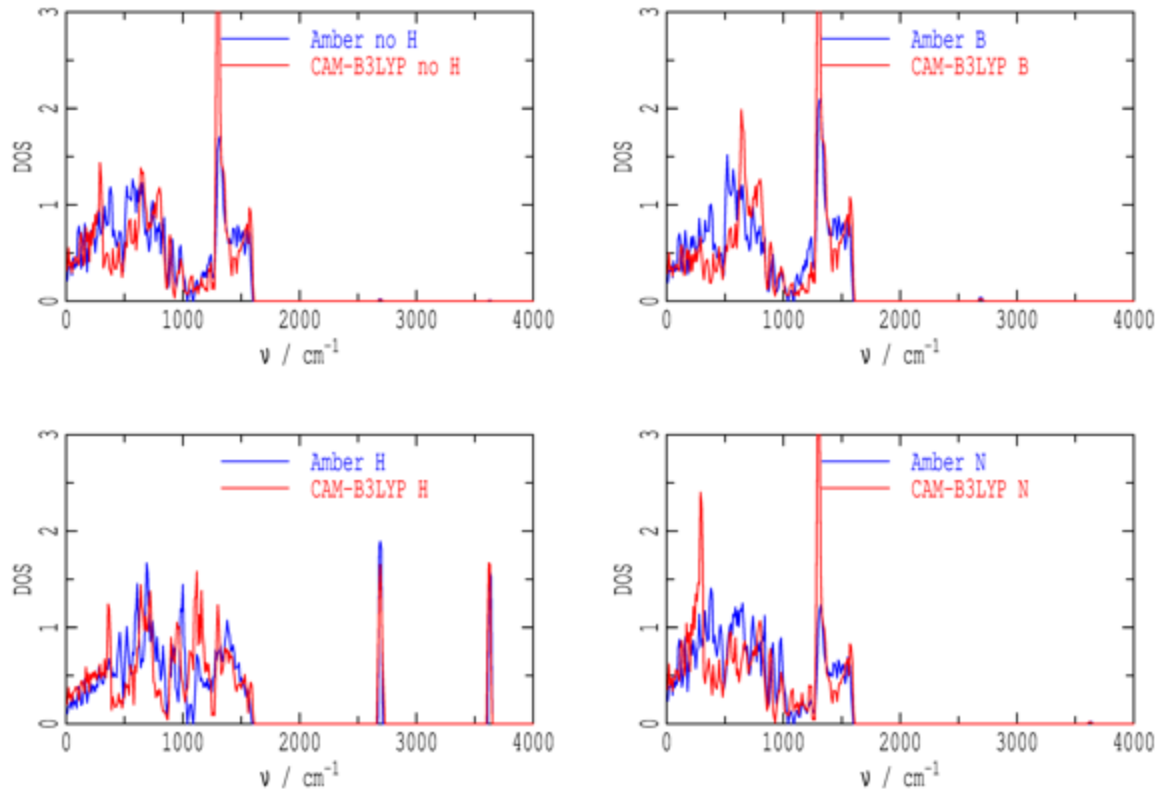
Figure S16. Density of vibrational states calculated by CAM-B3LYP/6-31G* for a 5-ring model of hBN, compared to AMBER results used to fit the force constants. The DOS is projected on motions involving B, N, and H atoms, as well as everything excluding H.

d. Geometry optimization boundary constraints

The way that the boundary of the ring model compounds is treated has significant effect on out-of-plane warping, the vibrational DOS, and possibly also energetics. For smaller model compounds, unconstrained optimization is used. For the 10-ring compound, forcing the boundary to be commensurate with the hBN lattice could has advantages. Hence in some calculations we freeze the N and B atoms of the outer ring in 10-ring models, as well as their terminating hydrogens. Freezing can be hazardous, however, as use of a slightly approximate frozen geometry can induce warping. The van der Waals terms in the MM model make this a sensitive issue as they should be summed over the whole lattice, not just the atoms in the molecular model. Uneven summation of the van der Waals forces leads to tiny distortions in geometry, but these could have profound influences on perceived out-of-plane distortions.

e. Calculations for $V_B C_N^-$

Table SA summarizes a wide variety of calculations performed for $V_BC_N^-$. For these, key optimized Cartesian Coordinates are supplied in an SI Data Set. The calculation methods used include (TD-)CAM-B3LYP and (TD-)HSE06, plus QM/MM calculations performed using (TD-)CAM-B3LYP or (EOM-)CCSD as the high-level method on the inner one or two rings, and either AMBER or (TD-)CAM-B3LYP as the low-level method. The total number of rings used is either 3, 5, or 10, and either 1 or 3 hBN layers are used. Except where indicated, the 6-31G* basis set is used, and all energies are at geometries individually optimized using the indicated method.

The ground state of $V_BC_N^-$ is identified as the quartet state $(1)^4A_2$ in C_{2v} symmetry, with singly occupied a_1 (σ), b_1 (π) and b_2 (σ) orbitals. The lowest-energy doublet state appears to be of similar energy to the lowest-energy quartet excited states. Herein we do not consider the doublet manifold or aspects such as ODMR directly, instead focusing on possible absorption and emission properties of the quartet manifold.

All calculations indicate that the low-energy states in the quartet manifold present an intricate structure. At least 4 states may contribute to processes activated by optical excitation, labelled in C_{2v} symmetry as $(1)^4A_1, (1)^4B_1, (1)^4B_2,$ and $(2)^4B_2$. Out-of-plane distortions could present significant aspects of defect properties. In C_s symmetry, $(1)^4A_1$ and $(1)^4B_1$ can either lead to two structures named $(2)^4A'$ and $(1)^4A'$, respectively, or else lead to the same structure with perhaps mixed character. An interconnecting transition state located in the Franck-Condon may also be perceived. The symmetry, ordering and mixing of all of these states are subtle properties that are perceived differently by the various computational methods applied. The same situation applies for $(1)^4B_2$ and $(2)^4B_2$, as these become $(3)^4A''$ and $(2)^4A''$, respectively, if out-of-plane distortions occur. Conical intersections linking these states to the others are also perceived within the Franck-Condon region, increasing the complexity of the quartet manifold.

In Table S2, the effect of out-of-plane distortion is followed by listing in the left-hand columns calculated properties in C_{2v} symmetry and then on the right related ones in C_s symmetry. The term ΔE_{Cv2} tells the lowering of the energy associated with this distortion. A value of "0" indicates no distortion. Sometimes this is determined by optimizing in lower symmetry, with no energy lowering found. On smaller models, this is checked by determining that all vibration frequencies are real at the high-symmetry structure. Small imaginary frequencies leading to tiny distortions of well depth less that the zero-point energy are neglected.

Table S2. Calculated excited-state properties for models of $V_BC_N^-$, including adiabatic transition energies ΔE_0 and vertical absorption energy ΔE_v^A from the $(1)^4A_2$ ground state (this label becomes $(1)^4A''$ in C_s symmetry), absorption and emission reorganisation energies λ^A and λ^E, and oscillator strengths; states are shown at C_{2v} symmetry and after distortion to C_s symmetry with energy change ΔE_{C2v}.

Total Rings or cell	Method[d]	Layers	in C_{2v} symmetry (planar)						in C_s symmetry (non-planar)					
			State	ΔE_0 eV	ΔE_v^A eV	λ^A eV	λ^E eV	f_{osc}	State	ΔE_{C2v} eV	ΔE_0 eV	λ^A eV	λ^E eV	f_{osc}
3	CAM	1	$(1)^4A_2$	[0]	-	-	-	-	$(1)^4A''$	0	[0]	-	-	-
			$(1)^4B_2$	1.72	2.65	0.93	0.85	0.0001	$(2)^4A''$	-0.07	1.65	1.00	1.03	0.0005
			$(1)^4B_1$	1.98	2.45	0.47	0.34	0.25	$(1)^4A'$	-0.15	1.83	0.62	0.46	0.16
			$(1)^4A_1$	1.90	2.09	0.19	0.17	0	$(2)^4A'$	barrierless relaxation to $(1)^4A'$				
			$(2)^4B_2$	2.03	2.15	0.12	0.13	0.0001						
			$(2)^4A_1$		3.49			0						
			$(2)^4A_2$		3.59			0.0010						
			$(1)^2A_1$	2.18	-	-	-	-						
			$(1)^2B_2$		1.13[a]			0.0003[a]						
			$(1)^2A_2$		1.40[a]			0[a]						

			(2)²A₂	1.71[a]				0[a]						
			(1)²B₁	1.91[a]				0.0003[a]						
			(3)²A₂	3.54[a]				0[a]						
3	HSE06	1	(1)⁴A₂	[0]	-	-	-	-	(1)⁴A''	0	[0]	-	-	-
			(1)⁴B₂	1.48	2.34	0.86	0.78	0.0001	(2)⁴A''	-0.10	1.38	0.96	0.94	0.0006
			(1)⁴B₁	2.12	2.51	0.39	0.28	0.24	(1)⁴A'	-0.21	1.91	0.60	0.42	0.10
			(1)⁴A₁	1.74	1.93	0.19	0.18	0						
			(2)⁴B₂	1.88	2.02	0.13	0.14	0.0001						
			(2)⁴A₁	2.38	2.89	0.51	0.56	0.0047						
			(2)⁴A₂		2.79			0.0001						
5×3√3	HSE06/D3	1	(1)⁴A₂	[0]										
			(1)⁴B₁	2.22										
5×3√3	HSE06/D3	4	(1)⁴A₂	[0]										
		3D periodic	(1)⁴B₁	2.16			0.28							
			(1)⁴A₁	2.13			0.18							
3	EOM1/CAM	1	(1)⁴A₂	[0]					(1)⁴A''	x	x			
			(1)⁴B₂						(2)⁴A''		1.83		1.50	0.0017
			(1)⁴B₁						(1)⁴A'		1.78		0.37	0.16
3	CAM/6-31G/D3	3	(1)⁴A₂	[0]										
			(1)⁴B₁	1.98			0.35	0.11	(1)⁴A'	0[e]				
			(1)⁴A₁	2.1			0.17	0	(2)⁴A''	0[e]				
5	CAM	1	(1)⁴A₂	[0]	-	-	-	-	(1)⁴A''	0.000	[0]	-	-	-
			(1)⁴B₂	1.73	2.66	0.93	0.85	0.0001	(2)⁴A''	-0.09	1.64		1.01	0.0001
			(1)⁴B₁	2.03	2.48	0.45	0.33	0.27	(1)⁴A'	-0.17	1.86		0.46	0.16
			(1)⁴A₁	1.94	2.12	0.18	0.16	0						
			(2)⁴B₂	2.04	2.16	0.12	0.12	0.0001						
			(2)⁴A₁		3.48										
5	CAM2/AMBER	1	(1)⁴A₂	[0]	-	-	-	-	(1)⁴A''	0.000	[0]	-	-	-
			(1)⁴B₂	1.62			0.83	0.0001	(2)⁴A''	-0.04	1.58		0.94	0.0010
			(1)⁴B₁	1.97			0.32	0.18	(1)⁴A'	-0.07	1.90		0.41	0.14
10	CAM2/AMBER[b]	1	(1)⁴A₂	[0]	-	-	-	-	(1)⁴A''	-0.56	[0]	-	-	-
			(1)⁴B₂	1.75			0.83	0.0001	(2)⁴A''	-0.77	1.53		0.93	0.0008
			(1)⁴B₁	2.15			0.34	0.19	(1)⁴A'	-0.86	1.85		0.38	0.14
10	CAM2/AMBER[b]	3	(1)⁴A₂	[0]	-	-	-	-	(1)⁴A''	-1.46	[0]	-	-	-
			(1)⁴B₂	1.75			0.83	0.0000	(2)⁴A''	-1.42	1.63		0.84	0.0005
			(1)⁴B₁	2.17			0.37	0.19	(1)⁴A'		1.91		0.20	0.14
			(2)⁴B₂						(3)⁴A''		2.06		0.12	0.0001
10	EOM2/AMBER[c]	3							(1)⁴A''		[0]			
									(1)⁴A'		1.95		0.20	0.14
10	CAM2/AMBER	3							(1)⁴A''		[0]			
									(2)⁴A''		1.64		0.83	0.0001
									(1)⁴A'		2.03		0.30	0.11

a: transition in the doublet manifold. b: 10th ring constrained at near hBN lattice. c: at CAM2/AMBER optimized geometries. d: CAM is CAM-B3LP, EOM is EOM-CCSD, 6-31G* basis unless indicated otherwise; QM/MM calculations are represented as <high-level method> <nber. rings in high level> / <low-level method>. e: optimization in C_1 symmetry did not reveal a lower-energy structure.

For the ground state $(1)^4A_2$, CAM-B3LYP calculations on small-ring models predict C_{2v} symmetry, with a tiny distortion predicted for the 5-ring model. The QM/MM method for larger

rings predicts significant distortion, but the magnitude of the effect may be overestimated owing to shortcomings in the AMBER force field. For the excited state of greatest interest, $(1)^4B_1$, TD-CAM-B3LYP predicts an out of plane distortion to $(1)^4A'$ for the 3-ring 1-layer model, but the symmetry remains C_{2v} when the calculations are expanded to 3 layers.

To match our experiments, we seek a defect with its lowest-energy transition with an adiabatic transition energy ΔE_0 near 2.1 eV, a very small emission reorganization energy in the range 0.10 – 0.15 eV, and considerable oscillator strength, e.g., $f_{osc} > 0.1$. Only one of the four quartet excited states of $V_BC_N^-$ is predicted to have a transition to the ground state with suitable oscillator strength, $(1)^4B_1$, the state that becomes $(1)^4A'$ in C_s symmetry. Also, only one state is predicted to have a very small emission reorganisation energy, $(1)^4A_1$, the state that becomes $(2)^4A'$ in C_s symmetry. As these two states can mix, and as such mixing is very difficult for calculations to properly perceive, the observed scenario can be considered as a feasible option as portrayed by the calculations. Another required feature is that the lowest-energy excited state must be $(1)^4B_1$ (or, if distorted out-of-plane, $(1)^4A'$).

Considering the results in Table S2 in greater detail, for the 3-ring 1-layer defect model, calculations are performed using (TD-)CAM-B3LYP, (TD-)HSE06, and a QM/MM method using (EOM-)CCSD for the inner ring and (TD-)CAM-B3LYP for the outer two rings. The HSE06 energies are typically lower than those for CAM-B3LYP, which are lower than those obtained using EOM-CCSD. This pattern has been seen before, with HSE06 known to underestimate transition energies compared to CAM-B3LYP and *ab initio* methods,[36, 37, 38, 44] becoming a serious problem whenever charge transfer becomes involved in the spectroscopic transiton.[44] Calculated adiabatic transition energies are near 1.8-2.0 eV for $(1)^4B_1$, lower than that observed, but within range of possible computational errors. A more significant issue is the calculated emission reorganization energies λ^E, which are 0.28-0.35 eV in C_{2v} symmetry, increasing to over 0.4 eV for the 1-layer models that admit C_s distortion, all much larger than observed values (Table S1) of 0.10-0.15 eV.

Table S2 considers improvements to the CAM-B3LYP calculations obtained by using a 3-ring 3-layer model (with the basis set reduced to 6-31G and D3(BJ) dispersion terms added). For $(1)^4B_1$, the optimized geometry returns to C_{2v} symmetry, owing to confinement of the out-of-plane distortion within the neighboring layers, with the adiabatic transition energy of $\Delta E_0 = 1.98$ eV, close to the observed values, with the reorganization energy of $\lambda^E = 0.35$ eV, still much larger than the observed values. Note that $(1)^4B_1$ becomes the lowest-energy state in the 3-layer model, with, also of note, $(1)^4A_1$ having lower energy than $(1)^4B_2$. The QM/MM calculations performed using EOMCCSD as the high-level method and TD-CAM-B3LYP as the low-level method perceive also $(1)^4B_1$ as the lowest-energy excited state. All in all, the calculations are consistent with the actual emitting state being $(1)^4B_1$, as is required for $V_BC_N^-$ to be the primary SPE.

Expansion of the defect from 3-ring to 5-ring (1-layer) is also considered in Table S2. Almost no change to the (TD-)CAM-B3LYP results is predicted, indicating that the electronic structure of the defect appears well converged at the 3-ring size, as has been observed for other defects.[35, 36, 37] A feature of possible significance, however, is the appearance of a very small imaginary frequency for the $(1)^4A_2$ ground state, suggesting that larger models could support out-of-plane distortion. The AMBER MM force field was developed to explore such possibilities. In test calculations Table S2 shows that a QM/MM approach using (TD-)CAM-B3LYP for the inner two rings and AMBER for the outer three leads to very similar results as does the pure (TD-)CAM-B3LYP ones.

The remaining results presented in Table S2 are for 10-ring models using QM/MM procedures, with either 1 or 3 hBN layers present. Figure S17 displays the 10-ring 1-layer model for $V_BC_N^-$ in C_{2v} symmetry viewed from above, and the 10-ring 3-layer distorted model predicted by QM/MM calculations. Interpretation of these results is clouded somewhat by the previously mentioned feature that the MM model predicts that hBN undergoes out-of-plane distortions, like what has been observed for graphene but on a much smaller length scale. The imaginary frequency reported for the 5-ring model from the CAM-B3LYP calculations suggest also that the effect may be qualitatively reasonable, but it is unclear as to whether or not the small size of the distortion predicted by QM/MM is reasonable or not. Nevertheless, as the hBN defects of interest were produced by bombardment with particle beams, and as defects located near crystal surfaces and phase edges are implicated in single-photon emission, the results obtained are indicative of effects that could somehow become relevant. The asymmetry in the response of the two neighboring layers is particularly suggestive of possible defect-location effects.
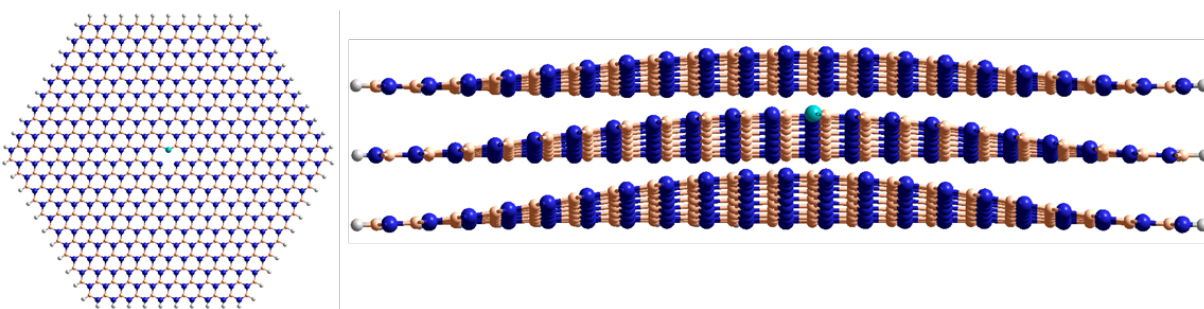
Figure S17—10 ring model of $V_BC_N^-$ showing the 1-ring C_{2v} structure in plan view (left) and the out-of-plane large-scale distorted QM/MM structure from the side (right), sectioned through the middle. *N- blue, B- peach, C- cyan.*

Of particular note, the large out-of-plane distortions predicted by the 10-ring 1-layer QM/MM model using (TD-)CAM-B3LYP and AMBER result in calculated adiabatic transition energies and emission reorganization energies of 1.85 eV and 0.38 eV for $(1)^4A' \rightarrow (1)^4A''$, respectively. Addition of two surrounding layers changes these to 1.91 eV and 0.20 eV, respectively, closer to the observed values. Single-point energies at these geometries obtained using (EOM-)CCSD instead of (TD-)B3LYP in the high QM/MM level yield very similar results, 1.95 eV and 0.20 eV, respectively, supporting the conclusions reached. In these calculations, the outer hBN ring was frozen at coordinates close to that expected for a pristine hBN lattice, which is found to enhance the out-of-plane distortion. With this condition relaxed, the (TD-)CAM-B3LYP with AMBER calculations continue to change the transition energy towards that observed, becoming 2.03 eV, but the reorganization energy becomes 0.30 eV, significantly further removed.

In Figure 5, two simulated spectra are presented. The solid line is that predicted by CAM-B3LYP using the basic 3-ring 1-layer model at C_{2v} symmetry and is expected to be very similar to that for the fully-optimized 3-ring 3-layer model. The emission reorganization energy from the calculations is $\lambda^E = 0.34$ eV, but the curvilinear-coordinated harmonic approximation[33, 60] used in the Huang-Rhys spectral simulations overestimates this as 0.36 eV (see Supporting Data). Nevertheless, this result is considered to be indicative of those perceived by more advanced computational methods, including the 3-ring 3-layer out-of-plane distorted CAM-B3LYP prediction of $\lambda^E = 0.37$ eV, the same as that from the EOM-CCSD1/CAM-B3LYP QM/MM calculation. Shown also in Figure 5, dashed, is that calculated spectrum scaled for the reduction

in reorganization energy to 0.20 eV predicted by both CAM-B3LYP2/AMBER and EOM-CCSD2/AMBER calculations for highly distorted structures, presenting results not out of the realms of possibility.

In summary, the various calculations presented perceive the low-energy quartet manifold of $V_BC_N^-$ in quite different ways. None of these ways straightforwardly corresponds to all of the spectroscopic and photochemical properties that we observe, yet the observed scenario is not implausible. The most significant shortcoming is that the state with predicted intense emission has an emission reorganization energy predicted to be in the range of $0.20 - 0.46$ eV, much larger than the observed range of $0.10 - 0.15$ eV. One relevant feature is that the observed values reflect contributions only from optical phonons, excluding acoustic phonons, whereas the calculated values embody both. This effect alone could not explain the discrepancy, however. Also, CAM-B3LYP calculations have been found to overestimate emission reorganization energies by similar magnitudes compared to experiment for the V_B^- defect, with in that case EOM-CCSD results predicting significantly narrower photoemission.[37] Another feature of note is that the calculated reorganization energies are, in the big picture, all quite small: defects can facilitate rearrangements of chemical boding on photoexcitation, often generating large reorganization energies of 2 eV or much more,[37, 38] with indeed some large values are reported in Table S2 and in subsequent tables for other defects. Accurate predictions for defects with small emission reorganization energies under 0.3 eV therefore poses a significant computational challenge. A related issue concerns how calculations can model the extreme bandshape changes observed in Regions I and II.

f. Calculations for V_NC_B

Before discussing extensive calculations on this defect candidate, which are merited given previous suggestions that it is a good match for the observed visible region emission, we note that we can conclusively rule out this defect upon our calculations. Its ground state is predicted [61, 62] to be $(1)^1A'$ with the lowest-energy triplet state predicted to be 1.2 eV higher in energy by CCSD. Hence the $(2)^3B_1 \rightarrow (1)^3B_1$ emission must follow absorption within the singlet manifold. The defect's photochemical cycle must therefore involve absorption, intersystem crossing, triplet emission, and then ground-state recovery. All calculations [61] indicate that this photocycle is not feasible as energy must be released as heat in three separate steps, with the sum of the heat released needing to be less than the difference between the laser excitation energy (2.33 eV) and the peak in emission (2.13 eV). Note that, in addition, such a photocycle would be extremely inefficient, contradictory to the bright emission observed experimentally. Furthermore, the $(2)^3B_1$ state is predicted to undergo out-of-plane distortion [61] that leads to very broad emission centered at 1.2 eV (3-layer 3-ring model).

Key optimized Cartesian Coordinates are supplied in an SI Date Set. This defect has been the subject of several studies, considering it as a potentially useful, should it be able to be produced,[33, 38, 63, 64] but it also has key spectroscopic features of specific interest herein.[38, 64] Calculations have reported a singlet ground state $(1)^1A_1$ that is highly open-shell in nature, making approaches such as TD-DFT, and even more so DFT itself, quite challenging. For calibration purposes, results obtained using the CAM-B3LYP and HSE06 density functionals have previously been compared to analogous ones obtained using a variety of *ab initio* computational methods.[38] Within the singlet manifold, a weak low-energy emission $(1)^1B_1 \rightarrow (1)^1A_1$ was noted. The only other emission of interest is a double excitation $(2)^1A_1 \rightarrow (1)^1A_1$ predicted with a very weak and very broad; barrierless relaxation from C_{2v} symmetry to the ground state is also predicted, making $(2)^1A_1$

unlikely to contribute to any photoemission. More significant, however, is the lowest-energy emission in the triplet manifold, $(2)^3B_1 \rightarrow (1)^3B_1$, as its predicted energy, intensity, and reorganization energy make it worthy of consideration as a candidate for the origin of the observed carbon-doped defect spectra.[38, 64] An unattractive feature, however, was the large predicted singlet-triplet gap, meaning that the required singlet to triple intersystem crossing would be strongly endothermic after excitation at the wavelength used herein, 532 nm.

Here, previous work[38] is extended, using the 3-ring model compound and again both the CAM-B3LYP and HSE06 density functionals. From a technical perspective, a significant feature[38] is that the critical $(2)^3B_1$ state has the same symmetry as the ground state. Hence solutions based on the Kohn-Sham DFT method, in-principle, cannot be obtained, as this state should collapse back to $(1)^3B_1$. However, use of inadequate calculation convergence criteria can allow solutions to be obtained, allowing programs such as Gaussian-16 and VASP to produce solutions, but their meaning is always questionable.[38] Hence only TD-DFT can be reliably applied to model $(2)^3B_1$, and this is the approach taken herein. The results from CAM-B3LYP and HSE06 calculations are qualitatively similar and we focus on the CAM-B3LYP ones, as these are typically 0.4 eV closer to those obtained by *ab initio* methods for $V_N C_B$.[38] Results are summarized in Table S3.

Following previous reports using this and other density funionals,[38, 62] calculations using CAM-B3LYP predict that the $(1)^1A_1$ ground state undergoes a significant distortion to C_s symmetry, the energy changing by ΔE_{C2v} = -0.31 eV to form a minimum with $(1)^1A'$ electronic structure (Table S3). At C_{2v} symmetry, the lowest-energy singlet excited state is predicted to be $(1)^1B_1$, with an adiabatic $(1)^1B_1 \rightarrow (1)^1A'$ transition energy of ΔE_0 = 2.16 eV, close to the observed excitation energy and emission ZPL. However, the oscillator strength is far too weak at f_{osc} = 0.004, and the emission reorganisation energy is large at λ^E = 0.48 eV. Emission from within the singlet manifold is therefore not likely to account for the observed absorption and emission. The only other singlet transition predicted in the visible region, $(2)^1A_1 \rightarrow (1)^1A_1$, is a double excitation that involves two states of significant open-shell character and so is poorly depicted by DFT techniques.[38] The DFT results presented in Table S3, as well as those performed on 2D periodic models using HSE06, along with other calculations using multi-reference methods, indicate that this transition should be very broad and quite weak.

Within the triplet manifold, the ground state is predicted by CAM-B3LYP to be $(1)^3B_1$, this lying 0.91 eV above $(1)^1A'$. Vibrational calculations indicate one imaginary frequency, but optimisation in C_s symmetry results in an insubstantial energy lowering, and hence vibrational averaging over the zero-point motion will produce results indicative of C_{2v} symmetry. We thus continue to describe this state as $(1)^3B_1$. In C_{2v} symmetry, the lowest transition within the triplet manifold is predicted to be $(2)^3B_1 \rightarrow (1)^3B_1$ at ΔE_0= 1.73 eV, with an oscillator strength of 0.11 and a reorganisation energy of λ^E = 0.38 eV; such spectral properties are similar to those predicted by the same method for $V_B C_N^-$ and could account for the observed emission, but again λ^E would need to be greatly reduced. However, the energy supplied experimentally from the 532 nm excitation is 2.33 eV, whereas the calculated energy required to access $(2)^3B_1$ from $(1)^1A'$ is 2.95 eV (obtained as $1.73 + 0.91 - (-0.31)$ eV from entries in Table SB). Hence the calculated energies indicate that the likelihood that $V_N C_B$ is responsible for the observed photoemission is small.

Table S3. Calculated excited-state properties for the 3-ring, 1-layer and 3-layer models of $V_N C_B$, including adiabatic transition energies ΔE_0 and vertical absorption energy ΔE_v^A, absorption and emission reorganisation energies λ^A and λ^E, and oscillator strengths; states are shown at C_{2v} symmetry and after distortion to C_s symmetry with energy change ΔE_{C2v}.

Density Functional	Layers	in C_{2v} symmetry (planar)						in C_s symmetry (non-planar)						
		State	ΔE_0 eV	ΔE_v^A eV	λ^A eV	λ^E eV	f_{osc}	State	ΔE_{C2v} eV	ΔE_0 eV	ΔE_v^A eV	λ^A eV	λ^E eV	f_{osc}
CAM-B3LYP	1	$(1)^1A_1$	[0]	-	-	-	-	$(1)^1A'$	-0.31	[0]	-	-	-	-
		$(1)^1B_1$	1.74	2.16	0.42	0.48	0.0043							
		$(2)^1A_1^{\ c}$	2.19	5.22	3.03	6.24			barrierless relaxation to $(1)^1A'$					
		$(2)^1B_1$		3.60			0.0000							
		$(1)^3B_1$	0.91				-	$(1)^3A''$	0.000^a	1.22				-
		$(2)^3B_1$	1.73^b	2.22^b	0.49	0.38	0.11	$(2)^3A'$	-0.04	1.69^b	2.22^b	0.53	0.62	0.11
		$(1)^3A_2$		3.35^b			0.017							
CAM-B3LYP/D3^e	3	$(1)^1A_1$	[0]	-	-	-	-	$(1)^1A'$	-0.13	[0]	-	-	-	-
		$(1)^3B_1$	0.82						0					
		$(2)^3B_1$	1.76^b	2.24	0.52	0.48		$(2)^3A'$	-0.04	1.72^b			0.55	0.085
HSE06	1	$(1)^1A_1$	[0]	-	-	-	-	$(1)^1A'$	-0.38^d	[0]	-	-	-	-
		$(2)^1A_1^{\ c}$	1.82	4.55	2.73	6.01			barrierless relaxation to $(1)^1A'$					
		$(1)^1B_1$	1.39	1.78	0.39	0.40	0.0021							
		$(2)^1B_1$		3.42			0.0000							
		$(1)^3B_1$	0.65				-	$(1)^3A_1''$	0^a	1.03				-
		$(2)^3B_1$	1.66^b	1.81^b	0.15	0.12	0.12	$(2)^3A'$	-0.36	1.45^b	1.81^b	0.36	0.65	0.12
		$(1)^3A_2$		2.90^b										
HSE06/D3^e	3	$(1)^1A_1$	[0]	-	-	-	-	$(1)^1A'$	-0.18	[0]	-	-	-	-
		$(1)^3B_1$	0.59						0					
		$(2)^3B_1$	1.71^b			0.39	0.077	$(2)^3A'$	-0.20	1.50^b			0.38	0.078

a: The C_{2v} geometry one imaginary frequency at $2.9i$ cm^{-1} and $4.0i$ cm^{-1} for CAM-B3LYP and HSE06, respectively, that do not lead to any significant energy lowering, so the structures are essentially C_{2v}.

b: For transitions within the triplet manifold, to get the energy with respect to the ground singlet state add ΔE_0 for $(1)^3B_1$ or $(1)^1A_1''$, as appropriate.

c: Double excitation, evaluated from DFT energy differences instead of TDDFT. Other relevant data[38] include: HSE06 2D periodic simulation at C_{2v} symmetry: ΔE_0 = 2.46 eV, ΔE_v^A = 3.61 eV, and CASSCF f_{osc} = 0.0024.

d: HSE06 2D periodic simulation value -0.42 eV.

e: 6-31G basis; single-point energies using 6-31G* at the 6-31G optimized geometries differ by at most 0.10 eV.

Nevertheless, this result warrants further attention and, as HSE06 has previously been applied to this defect and its performance calibrated against *ab initio* approaches,[38] we also consider its predictions. Most results are qualitatively similar to those from CAM-B3LYP, with the out-of-plane stabilization energy of $(1)^1A_1$ increasing from 0.31 eV to 0.38 eV, the $(2)^3B_1 \rightarrow (1)^3B_1$ transition energy in C_{2v} symmetry changing in from 1.73 eV to 1.66 eV, and the emission reorganization energy becoming 0.12 eV, close to the observed optical phonon value, but the effect of the out-of-plane distortion on $(2)^3B_1$ increases considerably from -0.04 eV to -0.36 eV. The

energy required to access $(2)^3B_1$ from $(1)^1A'$ thus changes from 2.95 eV to 2.69 eV, getting within range of the experimental excitation energy of 2.33 eV, but previous calibration studies of these density functionals against *ab initio* results indicate that HSE06 significantly underestimates this energy.[38] Also, the HSE06 calculated adiabatic transition energy changes to 1.45 eV, distant from the observed value, and the reorganization energy becomes significantly increased by the out-of-plane distortion to 0.65 eV, very much larger than the observed bandwidth; the maximum of the emission band profile $\lambda^5 E(\lambda)$ is predicted by HSE06 to occur at $\Delta E_v^E = \Delta E_0 - \lambda^E = 0.80$ eV. Hence HSE06 also indicates that it is highly unlikely that V_NC_B is responsible for the observed photoemission.

The effect of neighboring layers on the out-of-plane distortion of $(2)^3B_1$ has been considered using 3-ring 3-layers models (Table S3). Previously for $V_BC_N^-$, encapsulation of the defect in this fashion eliminated out-of-plane distortion, but in this case the distortion is only reduced in magnitude. Broad emission is still predicted, and the predicted emission band maximum becomes 1.17 eV (CAM-B3LYP) and 1.12 eV (HSE06) still a very long way from the observed values.

If the CAM-B3LYP and HSE06 calculations were to contain some serious misrepresentation of the actual excited-states of V_NC_B, then the simplest way in which this could manifest would be if $(1)^3B_1$ formed the ground state instead of $(1)^1A_1$. To explore this possibility, we perform a range of *ab initio* calculations on the energy difference of a 2-ring 1-layer model compound, with results given in Table S4. Calculations performed at this level on other defects show energy differences mostly within 0.15 eV of those evaluated on larger compounds with triple-zeta basis sets and also 2D periodic models.[36] All calculation methods predict a substantial energy instability of the triplet state of over 1 eV. The *ab initio* methods used show convergence with respect to expansion of the electron correlation treatment from complete neglect in the Hartree-Fock (HF)[65] treatment at 0.86 eV to 1.27 eV at the level of second-order Møller-Plesset perturbation theory (MP2),[66] to 1.15 eV using coupled-cluster singles and doubles theory (CCSD),[67] with no change when perturbative corrected for triples excitations is also added (CCSD(T)).[68] These results parallel those obtained for a 1-ring model for which multireference configuration-interaction (MRCI) calculations gave similar answers to CCSD and CCSD(T).[38] As any out-of-plane relaxation in the singlet manifold would only enhance the tabulated energy differences, the computational evidence supporting a singlet ground state is very strong.

Table S4. Comparison of DFT and *ab initio* adiabatic energy differences ΔE_0 between the $(1)^3B_1$ state of V_NC_B and $(1)^1A_1$, evaluated all at CAM-B3LYP optimized geometries for the 2-ring model; the 6-31G* basis set is used for all calculations.

method	ΔE_0 / eV
CAM-B3LYP	1.03
HSE06	0.77
HF	0.86
MP2	1.27
CCSD	1.15
CCSD(T)	1.15

Comment on the just published work of Ali et al.

A work has just appeared that claims "conclusive proof" that V_NC_B is responsible for the observed photoluminescence that we report following excitation at 2.33 eV.[69] In this, HSE06 calculations are performed on a 2D model, with the primary results being, for structures constrained to C_{2v} symmetry, an adiabatic transition energy of $\Delta E_0 = 1.75$ eV and an emission reorganization energy of $\lambda^E = 0.11$ eV. Even though these results were obtained using empirical

DFT energy differences, they are very similar to the values for our model compound (Table S3) obtained using first-principles TDDFT approaches of 1.66 eV and 0.12 eV, respectively. Essential to their V_NC_B assignment[69] is the claim that HSE06 predicts both $(1)^1A_1$ and $(2)^3B_1$ to have C_{2v} symmetry. No evidence supporting these claims is presented, despite previous works strongly suggesting otherwise,[38, 62] as indeed Table S3 demonstrates. HSE06 predicts large energy changes as a result of these out-of-plane distortions, with severe consequences for predicted spectra. Figure S18 shows some representative photoemission spectra from Regions I and II after corrections and conversion to present the band profile unscaled by wavelength. The calculated spectrum in C_{2v} symmetry has similar shape to that from Region II, just located too low in energy by 0.4 eV, but the actual spectrum from the full HSE06 calculation is a very broad band centered 1 eV lower. Another critical aspect of the V_NC_B assignment is the proposal that the photocycle of the defect involves $(2)^1A_1 \leftarrow (1)^1A_1$ excitation, which is claimed to be "optically bright" without supporting evidence and contrary to previous reasoning[38, 64] and the results shown in Table S3. This is then postulated to be followed by intersystem crossing to $(2)^3B_1$, $(2)^3B_1 \rightarrow (1)^3B_1$ photoemission, and finally recovery to the $(1)^1A_1$ ground state. Their mechanism involves energy loss as heat in three stages: relaxation following the initial singlet excitation, energy loss during intersystem crossing, and energy loss on the final ground-state recovery. As our observed photoemission peaks around 2.13 eV and the excitation energy is 2.33 eV, only a total of 0.20 eV of energy is available to be released in heat as a result of *all* of the processes involved in the photocycle. Previous HSE06 calculations[38] on 2D models similar to those presented[69] indicate that *each* of the three stages of heat loss in the proposed mechanism should release far more energy than this. Hence HSE06 calculations actually predict a qualitative scenario that is very different to the one needed to support the proposed photocycle, strongly suggesting that this mechanism is *not* responsible for our observed photoemission.
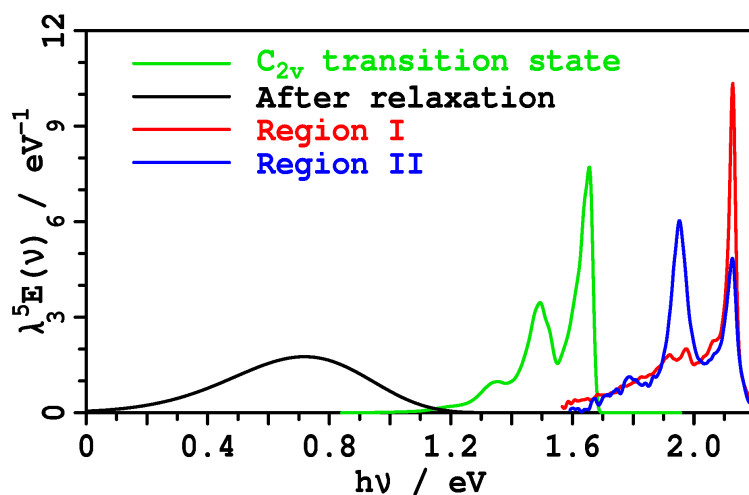
Figure S18. Sample observed spectral bandshapes $\lambda^5 E(\lambda)$ from Regions I (red) and II (blue), after correction for instrument response functions, are compared to simulated ones for V_NC_B, obtained using the Huang-Rhys approximation, for $(2)^3B_1 \rightarrow (1)^3B_1$ photoemission as predicted by HSE06/6-31G* calculations on the 3-ring model compound: green- at a C_{2v} transition state structure (very similar to that recently reported[69] using a 2D periodic 1-layer model, with the structure claimed therein to be predicted by HSE06 to be an equilibrium structure instead), and black- full calculation for 1-layer model including out-of-plane relaxation. Table S3 indicates that 3-layer models predict the HSE06 emission spectrum changing to a broad band centered at 1.1 eV.

g. Calculations for V_BC_N, $V_BC_N{}^+$, $V_NC_B{}^-$, $V_NC_B{}^+$, C_N, $C_N{}^+$, and $C_N{}^-$, C_B, $C_B{}^+$, and $C_B{}^-$

No transitions of significant oscillator strength that, within an error margin of 0.5 eV, could possibly form the lowest excited state in an energetically reachable spin manifold were identified for any of these defects. Note that C_N, proposed elsewhere as a candidate for the observed ODMR contrast,[8] is among those discarded due to its low oscillator strength (and thus long lifetime), one of the most reliable features of the calculation.

We start by considering key results obtained for the defects containing vacancies that are summarized in Table S5. V_BC_N appears to be difficult to study as it features multiple low-energy minima with very different geometries. The lowest-energy structure found after several searches was $(1)^3A_2$ in C_{2v} symmetry; this appears at 1.41 eV lower energy than that for $(1)^3B_2$, which has been previously identified as its ground state.[64] At vertical excitation, 5 excited states were predicted between 1.5 and 3.0 eV, but none with any significant oscillator strength. Besides $(1)^3B_2$, another low-energy excited state was also identified, $(1)^3A_1$ at 1.40 eV. A critical feature of this defect is, however, that large out-of-plane distortions are predicted for both $(1)^3A_2$ (making the ground state -1.7 eV lower in energy) and $(1)^3B_2$. As a consequence, the adiabatic emission is described best as $(2)^3A'' \rightarrow (1)^3A''$ in C_s symmetry at $\Delta E_0 = 0.89$ eV with $f_{osc} = 0.0001$. In addition, an unrelated state at a very different geometry $(1)^3A'$ was identified that had a relative energy of 0.59 eV. This state is not included in Table S5 as it involves an unrealistic degree of warping, driven by N-N bond formation to heal the defect, and is unlikely to pertain to any current experimental scenario. In summary, these properties indicate that this defect could not be responsible for the observed emission.

For $V_BC_N{}^+$, the ground state is predicted to be $(1)^2B_1$ when constrained to C_{2v} symmetry. It has a forbidden low-energy vertical excitation $(1)^2A_1 \rightarrow (1)^2B_1$ at 0.57 eV, making it a very unlikely candidate, and no alternatives are identified. Its lowest quartet state is predicted to be $(1)^4A_1$ at 3.19 eV and hence the quartet manifold is also not likely to be relevant to the experiments.

$V_NC_B{}^-$ has been previously considered as a possible defect.[63] CAM-B3LYP calculations predict its ground state to be $(1)^2B_1$ in C_{2v} symmetry, with of particular interest, an intense vertical absorption $(2)^2B_1 \rightarrow (1)^2B_1$ at 1.64 eV with $f_{osc} = 0.18$ that could be associated with the observed photoemission. In addition, however, a low-energy very weak absorption $(1)^2A_1 \leftarrow (1)^2B_1$ is also predicted at a vertical excitation energy of 1.02 eV. The presence of such a dark state would make the doublet manifold of $V_NC_B{}^-$ unlikely to be associated with the observed emission. The lowest quartet state of $V_NC_B{}^-$ is predicted to be $(1)^4A_1$ in C_{2v} symmetry at an energy that is 1.18 eV above $(1)^2B_1$. It is predicted to undergo an inconsequential distortion, lowering the symmetry to C_s. Ten excited state are predicted to be between 2.0 and 3.0 eV higher than this in energy, none with substantial oscillator strength. The large doublet to quartet energy gap, and the unavailability of significantly intense transitions, make emission following intersystem crossing an unlikely mechanism for the explanation of the observed spectra.

For $V_NC_B{}^+$, calculations predict a $(1)^2A_1$ ground state supporting a weak vertical absorption $(1)^2B_1 \leftarrow (1)^2A_1$ at 2.64 eV, with $f_{osc} < 0.00005$. A strong absorption is predicted to be $(2)^2A_1 \leftarrow (1)^2A_1$ at 3.79 eV with $f_{osc} < 0.24$, which is seemingly well outside the range of interest herein. The lowest quartet state is predicted to be $(1)^4B_2$ at the high energy of 3.96 eV and is therefore also unlikely to be involved in the observed emission; transition energies within the quartet manifold are also predicted to be very low, with three between $0.8 - 1.2$ eV.

Table S5. Calculated excited-state properties for the 3-ring, 1-layer defect model, including adiabatic transition energies ΔE_0 and vertical absorption energy ΔE_v^A, absorption and emission reorganization energies λ^A and λ^E, and oscillator strengths; states are shown at C_{2v} symmetry and after distortion to C_s symmetry with energy change ΔE_{C2v}. Transitions with oscillator strength sufficient to be compatible with the observed emission are emboldened.

Defect	in C_{2v} symmetry (planar)						in C_s symmetry (non-planar)						
	State	ΔE_0 eV	ΔE_v^A eV	λ^A eV	λ^E eV	f_{osc}	State	ΔE_{C2v} eV	ΔE_0 eV	ΔE_v^A eV	λ^A eV	λ^E eV	f_{osc}
$V_B C_N$	$(1)^3A_2$	[0]	-	-	-	-	$(1)^3A''$	-1.07	[0][a]		-	-	-
	$(1)^3A_1$	1.40	1.50	011	0.11	0	$(1)^3A'$	-1.58	0.89			0.35	0.0001
	$(1)^3B_2$	1.41	1.71	0.30	0.11	0.0001							
	$(2)^3B_2$		2.78			0.0002							
	$(3)^3B_2$		2.85			0.0002							
	$(1)^3B_1$		2.93			0.0161							
	$(1)^1A_1$	1.57	-	-	-	-							
	$(1)^1B_1$		1.18[a]			00002							
	$(1)^1A_2$		2.12[a]			0							
	$(2)^1B_1$		2.21[a]			0.0002							
	$(2)^1A_2$		2.94[a]			0							
	$(3)^1A_2$		4.07[a]			0							
$V_B C_N^+$	$(1)^2B_1$	[0]	-	-	-	-							
	$(1)^2A_1$		0.57			0.0000							
	$(1)^2B_2$		1.92			0.0000							
	$(2)^2B_1$		2.95			0.075							
	$(1)^4A_1$	3.19	-	-	-	-							
$V_N C_B^-$	$(1)^2B_1$	[0]	-	-	-	-	$(1)^2A'$	-0.10	[0]	-	-	-	-
	$(1)^2A_1$		1.02			0.0000							
	$(2)^2B_1$		1.64			**0.18**							
	$(2)^2A_1$		2.16			0.0001							
	$(1)^4A_1$	1.18	-	-	-	-	$(1)^4A'$	-0.01	-	-	-	-	-
	$(1)^4B_2$		2.03			0.014							
	$(2)^4B_2$		2.30[a]			0.0003							
	$(2)^4A_1$		2.37[a]			0.0008							
	$(3)^4A_1$		2.42[a]			0.0012							
	$(3)^4B_2$		2.45[a]			0.0015							
	$(4)^4A_1$		2.54[a]			0.0532							
	$(5)^4A_1$		2.66[a]			0.0009							
	$(4)^4B_2$		2.72[a]			0.049							
	$(6)^4A_1$		2.83[a]			0.0224							
	$(5)^4B_2$		2.93[a]			0.0557							
$V_N C_B^+$	$(1)^2A_1$	[0]	-	-	-	-							
	$(1)^2B_1$		2.64			0.0000							
	$(2)^2A_1$		3.79			**0.24**							
	$(1)^2A_2$		3.95			0							
	$(1)^4B_2$	3.96	-	-	-	-							

$(1)^4A_1$	0.79^a	0.025
$(2)^4B_1$	1.12^a	0.086
$(2)^4B_2$	1.16^a	0.049

a: with respect to the ground state for that spin manifold.

CAM-B3LYP predictions for defects with only atom substitutions and no vacancies are summarized in Table S6; results are similar to those from previous calculations.[35, 64] The ground state of C_N is predicted to be $(1)^2A_2''$, with all frequencies real in D_{3h} symmetry. The lowest quartet state is predicted to be 7.6 eV higher in energy. In the doublet manifold, the first excited state is predicted to be the Jahn-Teller active state $(1)^2E'$, which distorts to local minima of form $(1)^2B_2$ at an adiabatic transition energy of $\Delta E_0 = 2.26$ eV, with associated $(1)^2A_1$ transition states just 0.02 eV higher. The reorganisation energies to the minima are $\lambda^E = 0.45$ eV. Even though the Jahn-Teller distortion induces transition intensity, the calculated oscillator strength remains low, with $f_{osc} < 0.00005$. The only other low-energy transition is $(1)^2A_1'' \rightarrow (1)^2A_2''$ at $\Delta E_0 = 2.67$ eV, but this out-of-plane allowed transition also has $f_{osc} < 0.00005$. Hence it is highly unlikely that C_N could account for the observed emission.

C_N^- is isoelectronic with hBN and hence has a large band gap. The lowest-energy vertical excitation is predicted to be $(1)^1E' \leftarrow (1)^1A_1'$ at 5.12 eV, with a large oscillator strength of $f_{osc} = 0.30$; the associated triplet state is at 4.65 eV. Owing to the large band gap, this defect could not account for the observed emission.

Alternatively, C_N^+ is predicted to have a small band gap, with many low-energy states in both its singlet and triplet manifolds. Its ground state is predicted to be $(1)^1A_1'$, but this state is likely to be very open-shell in nature[38] and hence details of the TDDFT calculations may be unreliable.

The ground state of C_B is predicted to be $(1)^2A_2''$ in D_{3h} symmetry, with a small distortion occurring to C_{3v}. Three transitions are predicted to occur at under 3 eV energy, but all have very little oscillator strength. This includes the $(1)^2A_1''$ state at $\Delta E_0 = 2.47$ eV, and the Jahn-Teller split components of the $(1)^2E''$ state with $(1)^2A_2$ minima at 2.42 eV and $(1)^2B_1$ transition states at 2.57 eV. The lowest quartet state is $(1)^4A$ is C_2 symmetry at 6.49 eV. Hence no viable options are presented by which the observed emission could arise from C_B.

Many low-energy singlet and triplet states are predicted for C_B^-, making this an unlikely candidate to explain the observed emission. The ground state, which is likely to be highly open-shell in nature,[38] is predicted to be $(1)^1A_1'$ in D_{3h} symmetry, leading to $(1)^1A_1$ in C_{3v} symmetry at 0.71 eV lower energy.

C_B^+ is isoelectronic with hBN and hence has a large band gap. The lowest-energy singlet vertical excitation is predicted to be $(1)^1E' \leftarrow (1)^1A_1'$ at 5.59 eV, with a large oscillator strength of 0.40. It is not feasible that this transition could account for the observed emission.

Photoemission has recently been observed from carbon-treated hBN that is very different to what is observed herein.[70] Photoluminescence is observed at high energies, like those predicted for C_N^- and C_B^+, and these defects should be considered more in this context.

Table S6. Calculated excited-state properties for the 3-ring, 1-layer defect model, including adiabatic transition energies ΔE_0 and vertical absorption energy ΔE_v^A, absorption and emission reorganisation energies λ^A and λ^E, and oscillator strengths; states are shown at C_{2v} symmetry and after distortion to C_s symmetry with energy change ΔE_{C2v}. Transitions with oscillator strength sufficient to be compatible with the observed emission are emboldened.

| | | in C_{2v} or D_{3h} symmetry (planar) | | | | | | in some other symmetry | | | | | | | |
Defect	State in D_{3h}	State after distn. to C_{2v}	ΔE_0 eV	ΔE_v^A eV	λ^A eV	λ^E eV	f_{osc}	Symm	State	ΔE_{lower} eV	ΔE_0 eV	ΔE_v^A eV	λ^A eV	λ^E eV	f_{osc}
C_N	$(1)^2A_2''$		[0]	-	-	-	-			0					
	$(1)^2E'$	$(1)^2B_2$	2.26	2.63	0.37	0.45	0								
		$(1)^2A_1$	2.28	2.63	0.35	0.41	0.0000			0					
	$(1)^2A_1''$		2.67	3.08	0.35	0.35	0								
	$(1)^4A_1''$			7.63	-	-	-								
C_N^-	$(1)^1A_1'$		[0]	-	-	-	-								
	$(1)^1E'$			5.12			**0.30**								
	$(1)^1A_1'$			5.17			0								
	$(2)^1E'$			5.42			0.090								
	$(1)^3E'$			4.65			-								
	$(1)^3A_1'$			5.08			-								
	$(2)^3E'$			5.19			-								
C_N^+	$(1)^1A_1'$		[0]	-	-	-	-			0					
	$(1)^1A_2'$			1.40			0								
	$(1)^1E'$			1.92			0.0000								
	$(1)^1E''$			2.12			0								
	$(1)^1A_2'$			2.14			0								
	$(2)^1E'$			2.15			**0.34**								
	$(1)^3A_2'$			1.06			-								
	$(1)^3E''$			1.50			-								
C_B	$(1)^2A_2''$		[0]	-	-	-	-	C_{3v}	$(1)^2A_1$	-0.04	-	-	-	-	-
	$(1)^2A_1''$	$(1)^2A_2^b$	2.47	2.79	0.32	0.31	0.0000								
	$(1)^2E''$	$(1)^2A_2^b$	2.42	3.04	0.62		0.0002	C_1	$(1)^2A$	-0.13		2.33			
		$(1)^2B_1^b$	2.57	3.04	0.47		0								
								C_2	$(1)^4A$			6.49	-	-	-	-
C_B^-	$(1)^1A_1'$		[0]	-	-	-	-	C_{3v}	$(1)^1A_1$	-0.71					
	$(1)^1A_2''$			1.28			0								
	$(2)^1A_2''$			1.52			0								
	$(1)^1E'$			1.53			0.0032								
	$(2)^1E'$			1.66			0.0042								
	$(1)^3A_2'$		0.59	1.02			-								
	$(1)^3E'$			1.26			-								
C_B^+	$(1)^1A_1'$		[0]	-	-	-	-								
	$(1)^1E'$			5.59			**0.40**								

$(2)^1A_1'$	5.96	0
$(1)^3E'$	5.09	-
$(1)^3A_1'$	5.77	-

b: both states in D_{3h} lead to the same electronic configuration in C_{2v} at different geometries.

h. Supplementary data

1) The normal modes, Duschinsky matrices, and displacement vectors are provided for the spectral simulation shown in Fig. 5 in file: VBCN3-_14A2_14B1_cam_631gs_curvi.txt

2) Optimized Cartesian coordinates and basic characterization (including the lowest vibration frequencies when available) are listed in file: coordinates.txt

The order of the coordinates is:

1. VBCN- 3-ring 1-layer CAM-B3LYP   C2v (1)4A2
2. VBCN- 3-ring 1-layer CAM-B3LYP   C2v (1)4B1
3. VBCN- 3-ring 1-layer CAM-B3LYP   C2v (1)4B2
4. VBCN- 3-ring 1-layer CAM-B3LYP   Cs (1)4A'
5. VBCN- 3-ring 1-layer CAM-B3LYP   Cs (2)4A"
6. VBCN- 3-ring 1-layer EOM1/CAM   C2v (1)4A2
7. VBCN- 3-ring 1-layer EOM1/CAM   Cs (1)4A'
8. VBCN- 3-ring 1-layer EOM1/CAM   Cs (2)4A"
9. VBCN- 3-ring 3-layer CAM-B3LYP/D3 C2v (1)4A2 6-31G
10. VBCN- 3-ring 3-layer CAM-B3LYP/D3 C2v (1)4B1 6-31G
11. VBCN- 10-ring 3-layer CAM2/AMBER   C2v (1)4A2 ring 10 frozen
12. VBCN- 10-ring 3-layer CAM2/AMBER   C2v (1)4B1 ring 10 frozen
13. VBCN- 10-ring 3-layer CAM2/AMBER   Cs (1)4A" ring 10 frozen
14. VBCN- 10-ring 3-layer CAM2/AMBER   Cs (1)4A' ring 10 frozen
15. VBCN- 10-ring 3-layer CAM2/AMBER   Cs (2)4A" ring 10 frozen
16. VBCN- 10-ring 3-layer CAM2/AMBER   C2v (1)4A2
17. VBCN- 10-ring 3-layer CAM2/AMBER   Cs (1)4A'
18. VBCN- 10-ring 3-layer CAM2/AMBER   Cs (2)4A"
19. VNCB 3-ring 1-layer CAM-B3LYP   C2v (1)1A1
20. VNCB 3-ring 1-layer CAM-B3LYP   C2v (2)1A1
21. VNCB 3-ring 1-layer CAM-B3LYP   Cs (1)1A'
22. VNCB 3-ring 1-layer CAM-B3LYP   C2v (1)3B1
23. VNCB 3-ring 1-layer CAM-B3LYP   C2v (2)3B1
24. VNCB 3-ring 1-layer CAM-B3LYP   Cs (2)3A'
25. VNCB 3-ring 3-layer CAM-B3LYP/D3 C2v (1)1A1 6-31G
26. VNCB 3-ring 3-layer CAM-B3LYP/D3 Cs (1)1A' 6-31G
27. VNCB 3-ring 3-layer CAM-B3LYP/D3 C2v (1)3B1 6-31G
28. VNCB 3-ring 3-layer CAM-B3LYP/D3 C2v (2)3B1 6-31G
29. VNCB 3-ring 3-layer CAM-B3LYP/D3 Cs (2)3A' 6-31G
30. VNCB 3-ring 1-layer HSE06   C2v (1)1A1
31. VNCB 3-ring 1-layer HSE06   C2v (2)1A1
32. VNCB 3-ring 1-layer HSE06   Cs (1)1A'
33. VNCB 3-ring 1-layer HSE06   C2v (1)3B1
34. VNCB 3-ring 1-layer HSE06   C2v (2)3B1
35. VNCB 3-ring 1-layer HSE06   Cs (2)3A'
36. VNCB 3-ring 3-layer HSE06/D3   C2v (1)1A1 6-31G
37. VNCB 3-ring 3-layer HSE06/D3   Cs (1)1A' 6-31G

38. VNCB   3-ring 3-layer HSE06/D3   C2v (1)3B1 6-31G
39. VNCB   3-ring 3-layer HSE06/D3   C2v (2)3B1 6-31G
40. VNCB   3-ring 3-layer HSE06/D3   Cs (2)3A' 6-31G
41. VNCB   2D 6x6 periodic HSE06   ~C2v (1)1A1
42. VNCB   2D 6x6 periodic HSE06   Cs (1)1A'
43. VBCN   3-ring 1-layer CAM-B3LYP   Cs (1)3A"
44. VBCN   3-ring 1-layer CAM-B3LYP   C2v (1)1A1
45. VBCN   3-ring 1-layer CAM-B3LYP   C2v (1)2B1
46. VBCN   3-ring 1-layer CAM-B3LYP   C2v (1)4A2
47. VNCB- 3-ring 1-layer CAM-B3LYP   Cs (1)2A'
48. VNCB- 3-ring 1-layer CAM-B3LYP   Cs (1)4A'
49. VNCB+ 3-ring 1-layer CAM-B3LYP   C2v (1)2A1
50. VNCB+ 3-ring 1-layer CAM-B3LYP   C2v (1)4B2
51. CN   3-ring 1-layer CAM-B3LYP   C2v (1)2A2"
52. CN   3-ring 1-layer CAM-B3LYP   C2v (1)2B2
53. CN   3-ring 1-layer CAM-B3LYP   C2v (1)2A1
54. CN-   3-ring 1-layer CAM-B3LYP   C2v (1)1A1'
55. CN-   3-ring 1-layer CAM-B3LYP   C2v (1)1A1'
56. CN+   3-ring 1-layer CAM-B3LYP   C2v (1)1A1'
57. CB   3-ring 1-layer CAM-B3LYP   C3v (1)2A1
58. CB   3-ring 1-layer CAM-B3LYP   C1 (1)2A
59. CB   3-ring 1-layer CAM-B3LYP   C2v (1)2B1
60. CB-   3-ring 1-layer CAM-B3LYP   C3v (1)2A1
61. CB-   3-ring 1-layer CAM-B3LYP   D3h (1)2A2'
62. CB+   3-ring 1-layer CAM-B3LYP   D3h (1)1A1'

References

1.   Wigger D, Schmidt R, Del Pozo-Zamudio O, Preuß JA, Tonndorf P, Schneider R, *et al.* Phonon-assisted emission and absorption of individual color centers in hexagonal boron nitride. *2D Materials* 2019, **6**(3).

2.   Feldman MA, Puretzky A, Lindsay L, Tucker E, Briggs DP, Evans PG, *et al.* Phonon-induced multicolor correlations in hBN single-photon emitters. *Physical Review B* 2019, **99**(2).

3.   Chugh D, Wong-Leung J, Li L, Lysevych M, Tan HH, Jagadish C. Flow modulation epitaxy of hexagonal boron nitride. *2D Materials* 2018, **5**(4).

4.   Jacobsohn LG, Schulze RK, Maia da Costa MEH, Nastasi M. X-ray photoelectron spectroscopy investigation of boron carbide films deposited by sputtering. *Surface Science* 2004, **572**(2-3)**:** 418-424.

5.   Le Normand F, Hommet J, Szörényi T, Fuchs C, Fogarassy E. XPS study of pulsed laser depositedCNxfilms. *Physical Review B* 2001, **64**(23).

6.   Yamamoto K, Koga Y, Fujiwara S. Binding Energies of Amorphous CN and SiCN Films on X-Ray Photoelectron Spectroscopy. *Japanese Journal of Applied Physics* 2001, **40**(Part 2, No. 2A)**:** L123-L126.

7.   Manson NB, Hedges M, Barson MSJ, Ahlefeldt R, Doherty MW, Abe H, *et al.* NV−–N+ pair centre in 1b diamond. *New Journal of Physics* 2018, **20**(11).

8.   Chejanovsky N, Mukherjee A, Kim Y, Denisenko A, Finkler A, Taniguchi T, *et al.* Single spin resonance in a van der Waals embedded paramagnetic defect. *https://arxivorg/abs/190605903* 2019.

9.   Kraus H, Soltamov VA, Fuchs F, Simin D, Sperlich A, Baranov PG*, et al.* Magnetic field and temperature sensing with atomic-scale spin defects in silicon carbide. *Sci Rep* 2014, **4:** 5303.

10.   Mendelson N, Xu ZQ, Tran TT, Kianinia M, Scott J, Bradac C*, et al.* Engineering and Tuning of Quantum Emitters in Few-Layer Hexagonal Boron Nitride. *ACS Nano* 2019, **13**(3)**:** 3132-3140.

11.   Stern HL, Wang R, Fan Y, Mizuta R, Stewart JC, Needham LM*, et al.* Spectrally Resolved Photodynamics of Individual Emitters in Large-Area Monolayers of Hexagonal Boron Nitride. *ACS Nano* 2019, **13**(4)**:** 4538-4547.

12.   Xia Y, Li Q, Kim J, Bao W, Gong C, Yang S*, et al.* Room-Temperature Giant Stark Effect of Single Photon Emitter in van der Waals Material. *Nano Lett* 2019, **19**(10)**:** 7100-7105.

13.   Grosso G, Moon H, Lienhard B, Ali S, Efetov DK, Furchi MM*, et al.* Tunable and high-purity room temperature single-photon emission from atomic defects in hexagonal boron nitride. *Nat Commun* 2017, **8**(1)**:** 705.

14.   Tran TT, Elbadawi C, Totonjian D, Lobo CJ, Grosso G, Moon H*, et al.* Robust Multicolor Single Photon Emission from Point Defects in Hexagonal Boron Nitride. *ACS Nano* 2016, **10**(8)**:** 7331-7338.

15.   Gottscholl A, Kianinia M, Soltamov V, Orlinskii S, Mamin G, Bradac C*, et al.* Initialization and read-out of intrinsic spin defects in a van der Waals crystal at room temperature. *Nature Materials* 2020.

16.   Zobelli A, Ewels CP, Gloter A, Seifert G. Vacancy migration in hexagonal boron nitride. *Physical Review B* 2007, **75**(9).

17.   Weston L, Wickramaratne D, Mackoit M, Alkauskas A, Van de Walle CG. Native point defects and impurities in hexagonal boron nitride. *Physical Review B* 2018, **97**(21).

18.   Breitweiser SA, Exarhos AL, Patel RN, Saouaf J, Porat B, Hopper DA*, et al.* Efficient Optical Quantification of Heterogeneous Emitter Ensembles. *ACS Photonics* 2019, **7**(1)**:** 288-295.

19.   Vogl T, Campbell G, Buchler BC, Lu Y, Lam PK. Fabrication and Deterministic Transfer of High-Quality Quantum Emitters in Hexagonal Boron Nitride. *ACS Photonics* 2018, **5**(6)**:** 2305-2312.

20.   Proscia NV, Shotan Z, Jayakumar H, Reddy P, Cohen C, Dollar M*, et al.* Near-deterministic activation of room-temperature quantum emitters in hexagonal boron nitride. *Optica* 2018, **5**(9).

21.   Vogl T, Doherty MW, Buchler BC, Lu Y, Lam PK. Atomic localization of quantum emitters in multilayer hexagonal boron nitride. *Nanoscale* 2019, **11**(30)**:** 14362-14371.

22.   Choi S, Tran TT, Elbadawi C, Lobo C, Wang X, Juodkazis S*, et al.* Engineering and Localization of Quantum Emitters in Large Hexagonal Boron Nitride Layers. *ACS Appl Mater Interfaces* 2016, **8**(43)**:** 29642-29648.

23.   Ziegler J, Klaiss R, Blaikie A, Miller D, Horowitz VR, Aleman BJ. Deterministic Quantum Emitter Formation in Hexagonal Boron Nitride via Controlled Edge Creation. *Nano Lett* 2019, **19**(3)**:** 2121-2127.

24.   Onodera M, Watanabe K, Isayama M, Arai M, Masubuchi S, Moriya R*, et al.* Carbon-Rich Domain in Hexagonal Boron Nitride: Carrier Mobility Degradation and Anomalous Bending of the Landau Fan Diagram in Adjacent Graphene. *Nano Lett* 2019, **19**(10)**:** 7282-7286.

25. Jungwirth NR, Calderon B, Ji Y, Spencer MG, Flatte ME, Fuchs GD. Temperature Dependence of Wavelength Selectable Zero-Phonon Emission from Single Defects in Hexagonal Boron Nitride. *Nano Lett* 2016, **16**(10)**:** 6052-6057.

26. Mackoit-Sinkevičienė M, Maciaszek M, Van de Walle CG, Alkauskas A. Carbon dimer defect as a source of the 4.1 eV luminescence in hexagonal boron nitride. *Applied Physics Letters* 2019, **115**(21).

27. Sontheimer B, Braun M, Nikolay N, Sadzak N, Aharonovich I, Benson O. Photodynamics of quantum emitters in hexagonal boron nitride revealed by low-temperature spectroscopy. *Physical Review B* 2017, **96**(12).

28. Shotan Z, Jayakumar H, Considine CR, Mackoit M, Fedder H, Wrachtrup J*, et al.* Photoinduced Modification of Single-Photon Emitters in Hexagonal Boron Nitride. *ACS Photonics* 2016, **3**(12)**:** 2490-2496.

29. Mendelson N, Doherty M, Toth M, Aharonovich I, Tran TT. Strain-Induced Modification of the Optical Characteristics of Quantum Emitters in Hexagonal Boron Nitride. *Adv Mater* 2020**:** e1908316.

30. Nikolay N, Mendelson N, Özelci E, Sontheimer B, Böhm F, Kewes G*, et al.* Direct measurement of quantum efficiency of single-photon emitters in hexagonal boron nitride. *Optica* 2019, **6**(8).

31. Jungwirth NR, Fuchs GD. Optical Absorption and Emission Mechanisms of Single Defects in Hexagonal Boron Nitride. *Phys Rev Lett* 2017, **119**(5)**:** 057401.

32. Herzberg G, Teller E. Schwingungsstruktur der Elektronenübergänge bei mehratomigen Molekülen. *Zeitschrift für Physikalische Chemie* 1933, **21**(1)**:** 410-446.

33. Sajid A, Ford MJ, Reimers JR. Single photon emitters in hexagonal boron nitride: A review of progress. *Rep Prog Phys* 2020, **83**(4)**:** 044501.

34. Einstein A. Strahlungs-Emission und -Absorption nach der Quantentheorie. *Verhandlungen der Deutschen Physikalischen Gesellschaft* 1916, **18:** 318–323.

35. Korona T, Chojecki M. Exploring point defects in hexagonal boron-nitrogen monolayers. *Int J Quantum Chem* 2019, **119**(14)**:** e25925.

36. Reimers JR, Sajid A, Kobayashi R, Ford MJ. Convergence of defect energetics calculations. *arXiv* 2020, **2006.16454**.

37. Reimers JR, Shen J, Kianinia M, Bradac C, Aharonovich I, Ford MJ*, et al.* The photoluminescence and photochemistry of the V_B^- defect in hexagonal boron nitride. *arXiv* 2020, **2006.16474**.

38. Reimers JR, Sajid A, Kobayashi R, Ford MJ. Understanding and Calibrating Density-Functional-Theory Calculations Describing the Energy and Spectroscopy of Defect Sites in Hexagonal Boron Nitride. *J Chem Theory Comput* 2018, **14**(3)**:** 1602-1613.

39. Heyd J, Scuseria GE, Ernzerhof M. Hybrid functionals based on a screened Coulomb potential. *J Chem Phys* 2003, **118**(18)**:** 8207-8215.

40. Krukau AV, Vydrov OA, Izmaylov AF, Scuseria GE. Influence of the exchange screening parameter on the performance of screened hybrid functionals. *J Chem Phys* 2006, **125**(22)**:** 224106.

41. Cai Z-L, Crossley MJ, Reimers JR, Kobayashi R, Amos RD. Density-functional theory for charge-transfer: the nature of the N-bands of porphyrins and chlorophylls revealed

through CAM-B3LYP, CASPT2, and SAC-CI calculations. *J Phys Chem B* 2006, **110:** 15624-15632.

42. Cai Z-L, Sendt K, Reimers JR. Failure of time-dependent density-functional theory for large extended pi systems. *J Chem Phys* 2002, **117:** 5543-5549.

43. Peach MJG, Benfield P, Helgaker T, Tozer DJ. Excitation energies in density functional theory: An evaluation and a diagnostic test. *J Chem Phys* 2008, **128**(4)**:** 044118.

44. Reimers JR, Kobayashi R, Ford MJ. Density functionals with asymptotic-potential corrections are required for the simulation of spectroscopic properties of defects in materials. *arXiv* 2020, **2006.16463**.

45. Yanai T, Tew DP, Handy NC. A new hybrid exchange-correlation functional using the Coulomb-attenuating method (CAM-B3LYP). *Chem Phys Lett* 2004, **393**(1-3)**:** 51-57.

46. Kobayashi R, Amos RD. The application of CAM-B3LYP to the charge-transfer band problem of the zincbacteriochlorin–bacteriochlorin complex. *Chem Phys Lett* 2006, **420:** 106–109.

47. Reimers JR, Cai Z-L, Kobayashi R, Rätsep M, Freiberg A, Krausz E. Assignment of the Q-Bands of the Chlorophylls: Coherence Loss via Qx - Qy Mixing. *Sci Rep* 2013, **3:** 2761.

48. Rätsep M, Linnanto JM, Muru R, Biczysko M, Reimers JR, Freiberg A. Absorption-emission symmetry breaking and the different origins of vibrational structures of the 1Qy and 1Qx electronic transitions of pheophytin a. *J Chem Phys* 2019, **151**(16)**:** 165102.

49. Rätsep M, Cai Z-L, Reimers JR, Freiberg A. Demonstration and interpretation of significant asymmetry in the low-resolution and high-resolution Qy fluorescence and absorption spectra of bacteriochlorophyll a. *J Chem Phys* 2011, **134**(2)**:** 024506.

50. Stanton JF, Bartlett RJ. The equation of motion coupled-cluster method. A systematic biorthogonal approach to molecular excitation energies, transition probabilities, and excited state properties. *J Chem Phys* 1993, **98:** 7029-7039.

51. Goerigk L, Grimme S. A thorough benchmark of density functional methods for general main group thermochemistry, kinetics, and noncovalent interactions. *Phys Chem Chem Phys* 2011, **13**(14)**:** 6670-6688.

52. Hehre WJ, Ditchfield R, Pople JA. Self-consistent molecular orbital methods. XII. Further extensions of gaussian-type basis sets for use in molecular orbital studies of organic molecules *J Chem Phys* 1972, **56:** 2257-2261.

53. Frisch MJ, Trucks GW, Schlegel HB, Scuseria GE, Robb MA, Cheeseman JR*, et al. Gaussian 16 Revision C.01*. Gaussian Inc.: Wallingford, CT, 2016.

54. Werner HJ, Knowles PJ, Amos RD, al. e. *MOLPRO*. University of Birmingham: Birmingham, 2007.

55. Svensson M, Humbel S, Froese RDJ, Matsubara T, Sieber S, Morokuma K. ONIOM: A Multi-Layered Integrated MO + MM Method for Geometry Optimizations and Single Point Energy Predictions. A Test for Diels-Alder Reactions and Pt(P(t-Bu)$_3$)$_2$ + H$_2$ Oxidative Addition. *J Phys Chem* 1996, **100:** 19357-19363.

56. Dapprich S, Komaromi I, S. BK, Morokuma K, Frisch MJ. A new ONIOM implementation in Gaussian98. Part I. The calculation of energies, gradients, vibrational frequencies and electric field derivatives. *J Mol Struct (THEOCHEM)* 1999, **461-462:** 1-21.

57. Cornell WD, Cieplak P, Bayly CI, Gould IR, Merz Jr KM, Ferguson DM, *et al.* A second generation force field for the simulation of proteins, nucleic acids, and organic molecules. *J Am Chem Soc* 1995, **117:** 5179-5197.

58. Weiner SJ, Kollman PA, Case DA, Singh UC, Ghio C, Alagona G, *et al.* A New Force Field for Molecular Mechanical Simulation of Nucleic Acids and Proteins. *J Am Chem Soc* 1984, **106:** 765-784.

59. Cheng-Rong H, Cheng C, Chou J-P, Chun-Ming C, Ching-Ming W. Van der Waals interaction in BN bilayer. *New J Phys* 2014, **16**(11).

60. Reimers JR. A practical method for the use of curvilinear coordinates in calculations of normal-mode projected displacements and Duschinsky rotation matrices for large molecules. *J Chem Phys* 2001, **115:** 9103-9109.

61. Reimers JR, Sajid A, Kobayashi R, Ford MJ. Understanding and Calibrating Density-Functional-Theory Calculations Describing the Energy and Spectroscopy of Defect Sites in Hexagonal Boron Nitride. *J Chem Theory Comput* 2018, **14**(3)**:** 1602-1613.

62. Noh G, Choi D, Kim J-H, Im D-G, Kim Y-H, Seo H, *et al.* Stark Tuning of Single-Photon Emitters in Hexagonal Boron Nitride. *Nano Lett* 2018, **18**(8)**:** 4710-4715.

63. Wu F, Galatas A, Sundararaman R, Rocca D, Ping Y. First-principles engineering of charged defects for two-dimensional quantum technologies. *Physical Review Materials* 2017, **1**(7)**:** 071001.

64. Sajid A, Reimers JR, Ford MJ. Defect states in hexagonal boron nitride: Assignments of observed properties and prediction of properties relevant to quantum computation. *Phys Rev B* 2018, **97**(6)**:** 064101.

65. Fock V. "Selfconsistent field" mit Austausch für Natrium. *Zeitschrift für Physik* 1930, **62**(11-12)**:** 795-805.

66. Møller C, Plesset MS. *Phys Rev A* 1934, **46:** 618.

67. Čížek J. On the Correlation Problem in Atomic and Molecular Systems. Calculation of Wavefunction Components in Ursell-Type Expansion Using Quantum-Field Theoretical Methods. *J Chem Phys* 1966, **45**(11)**:** 4256-4266.

68. Raghavachari K, Trucks GW, Pople JA, Head-Gordon M. A fifth-order perturbation comparison of electron correlation theories. *Chem Phys Lett* 1989, **157:** 479-483.

69. Ali S, Thygesen KS. VNCB defect as source of single photon emission from hexagonal boron nitride. *2D Materials* 2020, **in press** https://doi.org/10.1088/2053-1583/ab1088f1061.

70. Pelini T, Elias C, Page R, Xue L, Liu S, Li J, *et al.* Shallow and deep levels in carbon-doped hexagonal boron nitride crystals. *Phys Rev Mater* 2019, **3**(9)**:** 094001.